

Chapter 3

2-D Field Data Results

In 1997, WesternGeco distributed a 2-D dataset, acquired in the Mississippi Canyon region of the Gulf of Mexico, for the testing of multiple suppression algorithms. As illustrated on the CMP-stacked section, Figure 3.1, the data contain a variety of strong surface-related multiples which hamper primary imaging, and enough geologic complexity to render one-dimensional multiple suppression methods ineffectual.

In this chapter, I show the results of testing my particular implementation of the LSJIMP technique on 750 CMP locations of the Mississippi Canyon dataset, modeling four multiple generators—the seabed, two strong shallow reflectors, and the top of salt—as labeled by the picks on Figure 3.1. Only first order multiples are included in the inversion. Thus in equation (2.28), $n_{\text{surf}} = 4$ and $p = 1$.

Estimation of a multiple generator’s reflection coefficient is a crucially important step in my implementation of LSJIMP. Figures 3.2-3.5 illustrate the result of applying the reflection coefficient methodology outlined in Section 2.2.5 to each of the four multiple generators shown in Figure 3.1. Each Figure shows a stack of the local windows around the primary reflection and first pure multiple after alignment with cross-correlation, weighted by a user-defined residual weight which is set to zero where the data appear incoherent, and to one elsewhere. The seabed and R1 reflections (Figures 3.2 and 3.3) have the greatest coherency, with fairly consistent estimated reflection coefficients across all midpoints, although the R1

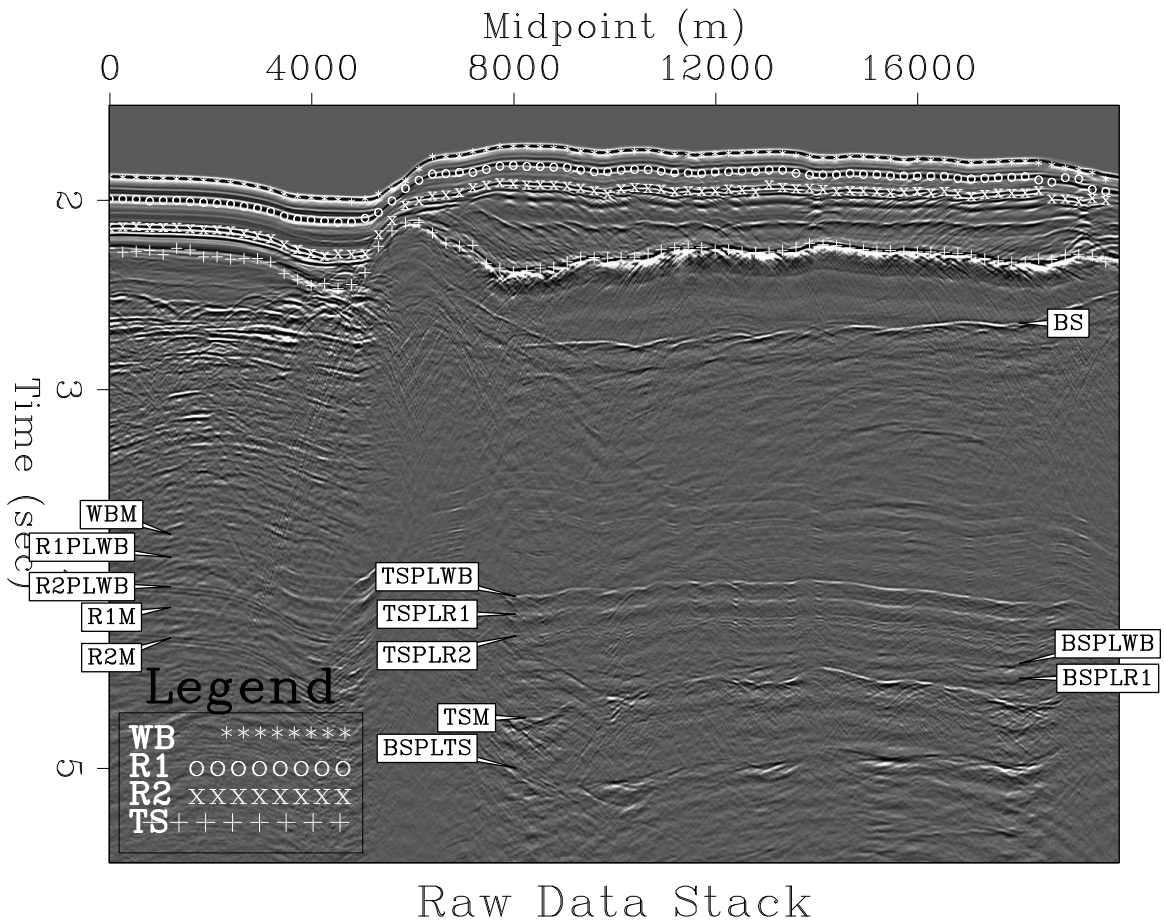


Figure 3.1: Stacked Mississippi Canyon 2-D dataset (750 midpoints), annotated with important multiple-generating horizons and multiples, after application of t^2 gain. Four multiple generators were modeled in the LSJIMP inversion: WB - seabed; R1,R2 - strong shallow reflections; TS - top of salt. Bottom of salt – BS, is also shown. Naming convention for pure first-order multiples: (*reflector*)M, e.g., R1M. Naming convention for first-order pegleg multiples: (*target*)PL(*multiple generator*), e.g., BSPLWB. results2d-gulf.stackraw [CR]

pure multiple partially overlaps the strong R2 seabed pegleg and tends to bias the estimated R1 reflection coefficient upward. The short wavelength of the multi-peaked R2 reflection (Figure 3.4) cause offset-dependent tuning effects that somewhat degrades our ability to reliably estimate a reflection coefficient. Lastly, strong head waves and a rugose salt top degrade the coherency of the top-of-salt reflection and its multiple (Figure 3.5), although we can get a fairly reliable estimate between midpoints of about 12000 and 18000 meters.

Figure 3.2: Top: Stack of window around seabed reflection (WB). Center: Stack of window around seabed pure multiple (WBM). Bottom: estimated WB reflection coefficient. `results2d-rc.1.gulf` [CR]

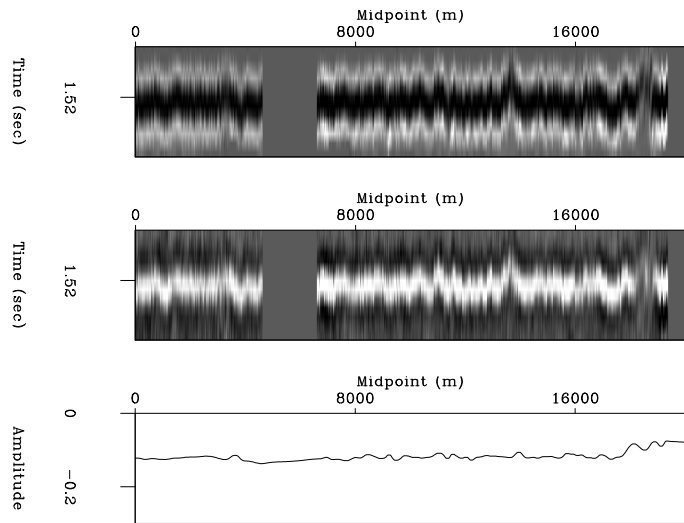
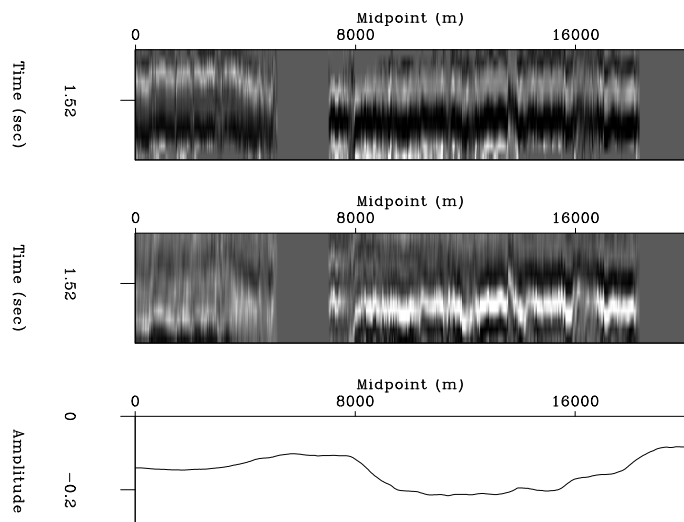


Figure 3.3: Top: Stack of window around R1 reflection. Center: Stack of window around R1 pure multiple (R1M). Bottom: estimated R1 reflection coefficient. `results2d-rc.2.gulf` [CR]



WesternGeco supplied a depth interval velocity model, so computation of stacking velocities was trivial. I ran LSJIMP with 20 conjugate gradient iterations on 28 CPUs (1.3 Ghz

Figure 3.4: Top: Stack of window around R2 reflection. Center: Stack of window around R2 pure multiple (R2M). Bottom: estimated R2 reflection coefficient. `results2d-rc.3.gulf` [CR]

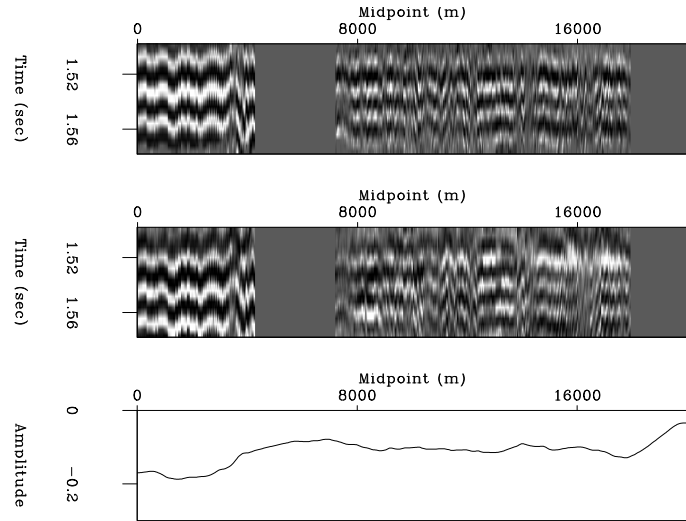
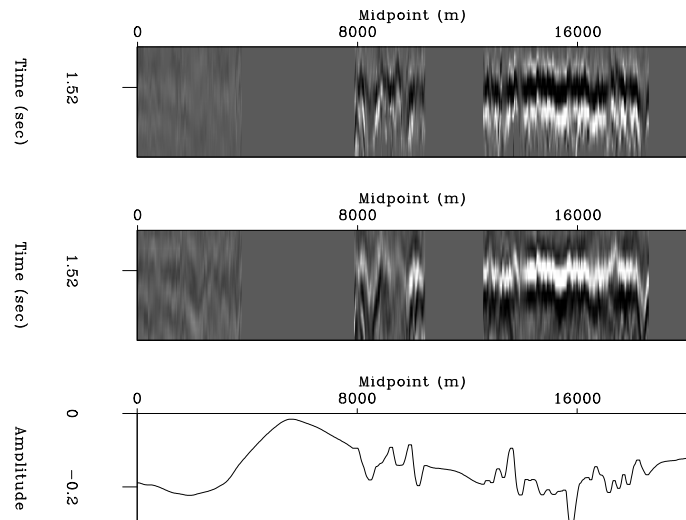


Figure 3.5: Top: Stack of window around top-of-salt reflection (TS). Center: Stack of window around top-of-salt pure multiple (TSM). Bottom: estimated TS reflection coefficient. `results2d-rc.4.gulf` [CR]



Pentium 3) of a Linux cluster, for a total run time of around 3 hours, including all I/O. Coincidentally, the run time is very similar to the prestack wave-equation depth migration run to generate the results in section 3.0.1.

Figure 3.6 illustrates the stack of the LSJIMP primary image, \mathbf{m}_0 , which should contain only primaries. From the difference panel (c), note that important above-salt peglegs are almost entirely removed. Primaries are not visibly damaged. Salt rugosity contributes negatively to the separation, by forming diffractions that are not modeled by HEMNO, and by violating HEMNO's small reflector dip assumption. Still, LSJIMP does a fairly good job of removing the specular components of strong salt-related multiples. Some deep multiple energy remains. While unmodeled multiple events, such as internal salt multiples, may explain the residual, another likely contributor is the complex subsalt wave propagation. Time imaging operators like HEMNO generally perform more poorly than depth migration below large velocity contrasts.

Figures 3.7 and 3.8 make the same comparison as Figure 3.6, but in small windows to emphasize local features. The geological context of Figure 3.7 is a generally well-behaved sedimentary basin, with shallow dips and low velocity contrast. Notice that a variety of strong peglegs are largely removed without badly damaging the many updipping primary events in the section. Figure 3.8 is taken from over the tabular salt body. The multiples visible in this window are effectively separated from the data, even those from the top and bottom of the salt. Weak subsalt primaries, like the anticlinal structure which peaks around CMP 16000 m are not visibly harmed by the separation.

Figures 3.9-3.11 show the LSJIMP results at three midpoint locations. In each Figure, panels (c), (d), (g), and (h) illustrate the estimated total first order multiple from each of the four multiple generators. For instance, to generate the estimated seabed pegleg panel (c), we construct a model vector,

$$\mathbf{m}_{wb} = \left[\mathbf{0} \quad \mathbf{m}_{1,0,1} \quad \mathbf{m}_{1,1,1} \quad \mathbf{0} \quad \mathbf{0} \quad \mathbf{0} \quad \mathbf{0} \quad \mathbf{0} \quad \mathbf{0} \right]^T, \quad (3.1)$$

where vector $\mathbf{0}$ has the same dimension as a CMP gather and vectors $\mathbf{m}_{1,0,1}$ and $\mathbf{m}_{1,1,1}$ are the images of the source and receiver peglegs from the seabed. To compute the estimated total

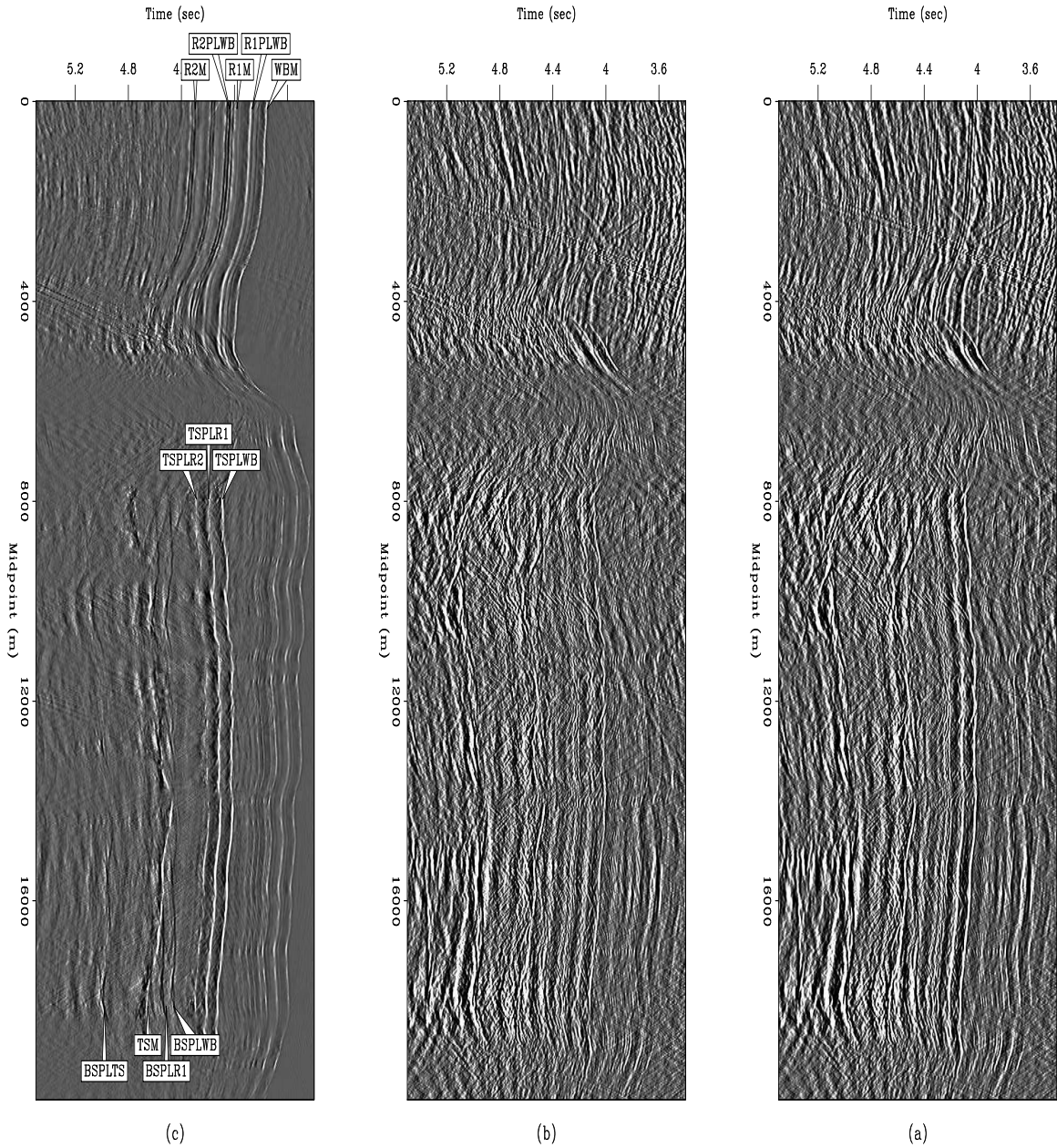


Figure 3.6: Mississippi Canyon stacked section before and after LSJIMP. All panels windowed in time from 3.5 to 5.5 seconds and gained with t^2 . (a) Raw data stack. (b) Stack of estimated primary image, \mathbf{m}_0 . (c) Stack of the subtracted multiples. Prominent multiples labeled as in Figure 3.1. [results2d-stackcomp.gulf](https://results2d-stackcomp.gulf.com) [CR,M]

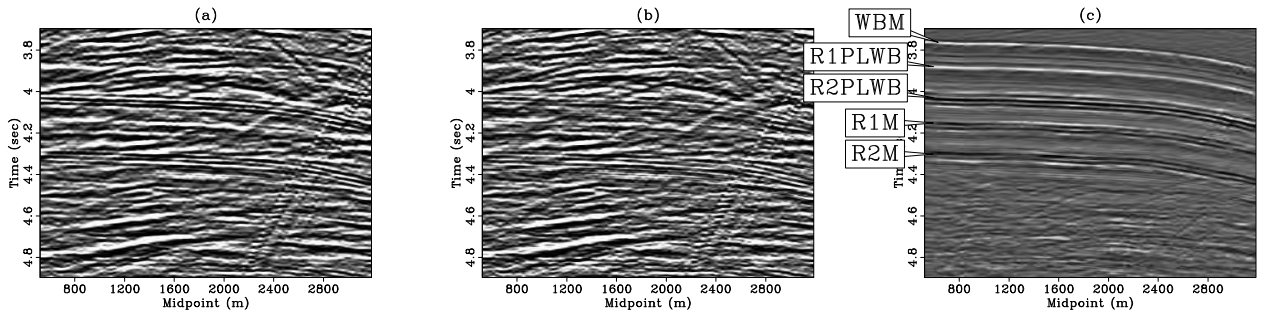


Figure 3.7: Zoom of Mississippi Canyon stacked section before and after LSJIMP. All panels windowed in time from 3.7 to 4.9 seconds and in midpoint from 500 to 3200 meters and gained with t^2 . (a) Raw data; (b) Estimated primaries (\mathbf{m}_0); (c) Stack of the subtracted multiples. Multiples labeled as in Figure 3.1. `results2d-stackcomp.zoom.1.gulf` [CR,M]

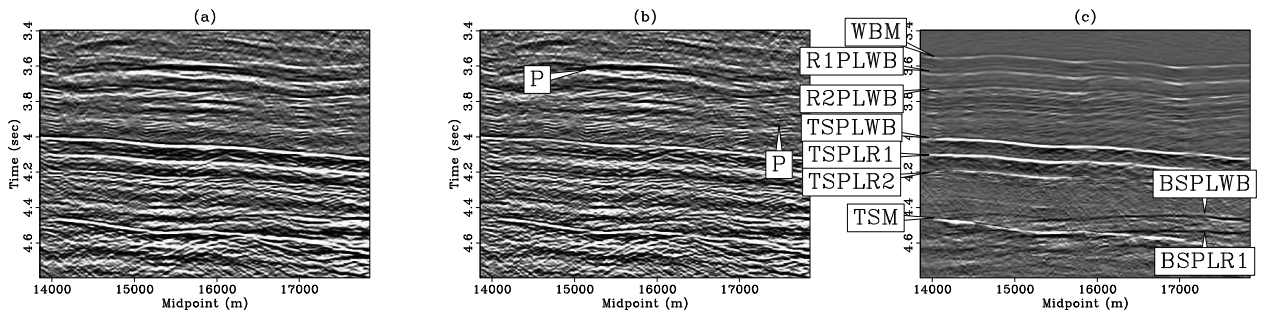


Figure 3.8: Zoom of Mississippi Canyon stacked section before and after LSJIMP. All panels windowed in time from 3.4 to 4.8 seconds and in midpoint from 13850 to 17850 meters and gained with t^2 . (a) Raw data; (b) Estimated primaries (\mathbf{m}_0); (c) Stack of the subtracted multiples. Multiples labeled as in Figure 3.1. Subsalt primary events labeled “P”. `results2d-stackcomp.zoom.3.gulf` [CR,M]

first-order seabed pegleg, we simply apply the LSJIMP forward model:

$$\mathbf{d}_{wb} = \mathbf{L}\mathbf{m}_{wb}. \quad (3.2)$$

An analogous process can be repeated for the first-order peglegs from the other three multiple generators modeled here. The modeled data (panel (e)) is simply the sum of the estimated primaries (panel (b)) and the first-order peglegs from the four modeled multiple generators. The residual error (panel (f)) is the difference between the input data and modeled data, with the residual weight applied to account for missing traces in the input.

Figure 3.9 comes from the sedimentary basin portion of the data. The multiples on this gather have fairly simple moveout behavior. From the relatively small amount of correlated energy on the residual error panel (f), we see that most multiples present in the data are modeled well by LSJIMP. However, notice the introduction of a “new” event to the modeled data around $\tau = 4.15s$. The R1M event overlaps with R2PLWB, which leads to crosstalk leakage and a poor estimate of R1’s reflection coefficient. As we will see later, in section 3.3, the nonlinear updating scheme of section 2.1.8 helps solve this problem.

Figure 3.10 is drawn from the left-hand side of the salt body. The separation results are quite good, both for the relatively simple shallow multiples and for the complex salt-related multiples, which visibly split. A flat event around 4.5 seconds, which appears to be a primary, is actually most likely a pegleg multiple from the base of salt, flattened because the stacking velocity decreases below the salt.

Figure 3.11 is drawn from the right-hand side of the salt body. As with Figure 3.10, some of the complex splitting behavior in the salt-related peglegs is effectively modeled by HEMNO. In this case, the reflector dips are such that the events split at medium offsets, but happen to coincide at far offsets. Signal events are quite difficult to spot under the multiples, but some shallow events are uncovered.

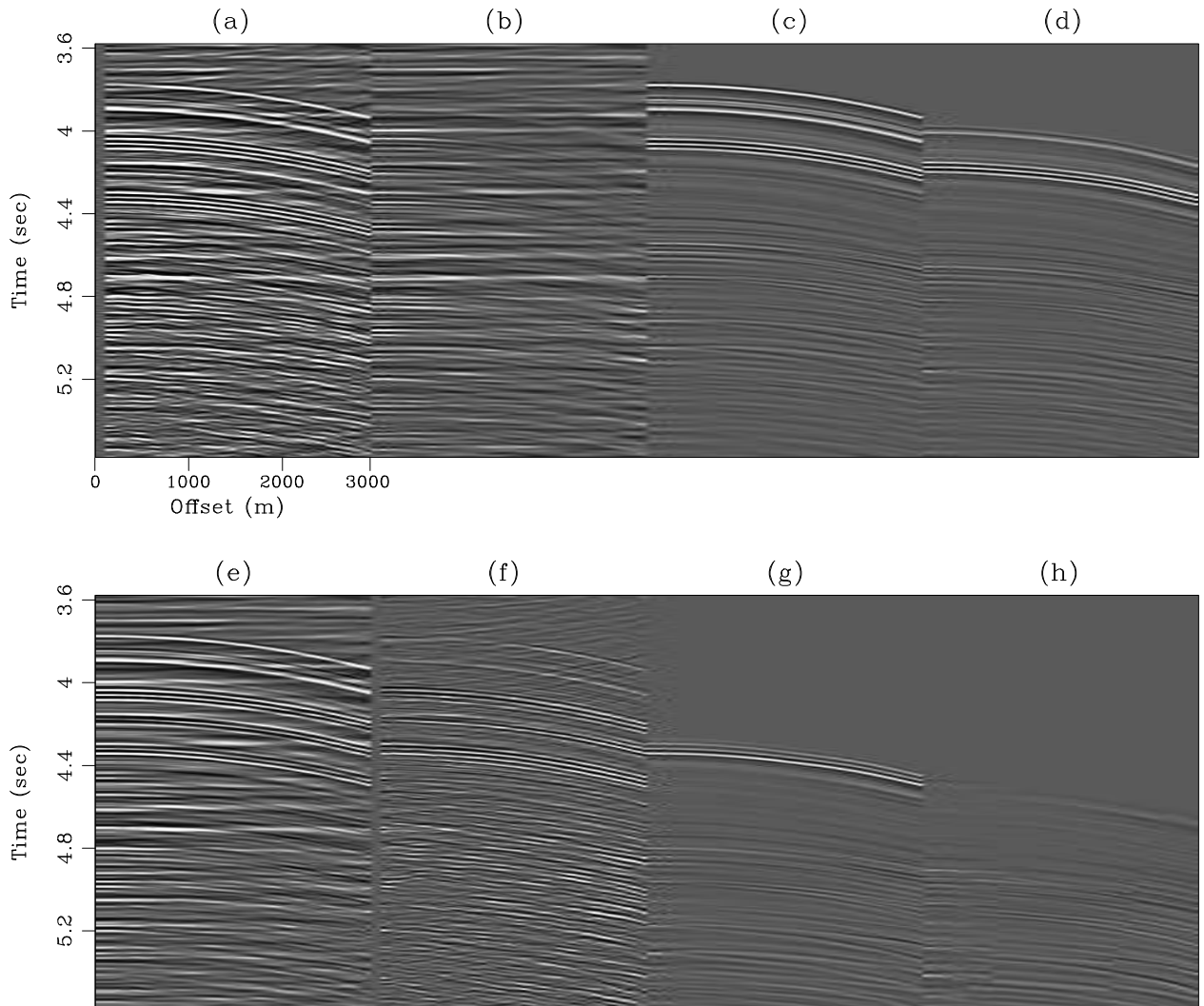


Figure 3.9: Mississippi Canyon CMP 55 (1440 m). Events labeled as in Figure 3.1. All panels NMO'ed with stacking velocity and windowed in time from 3.5 to 5.5 seconds and gained with t^2 . (a) Raw data; (b) Estimated primaries (m_0); (c) Estimated WB peglegs; (d) Estimated R1 peglegs; (e) Estimated data (sum of (b), (c), (d), (g), and (h)); (f) Data residual (difference of (a) and (e)); (g) Estimated R2 peglegs; (h) Estimated TS peglegs. [results2d-comp1.4.lsrow.gulf.55](#) [CR]

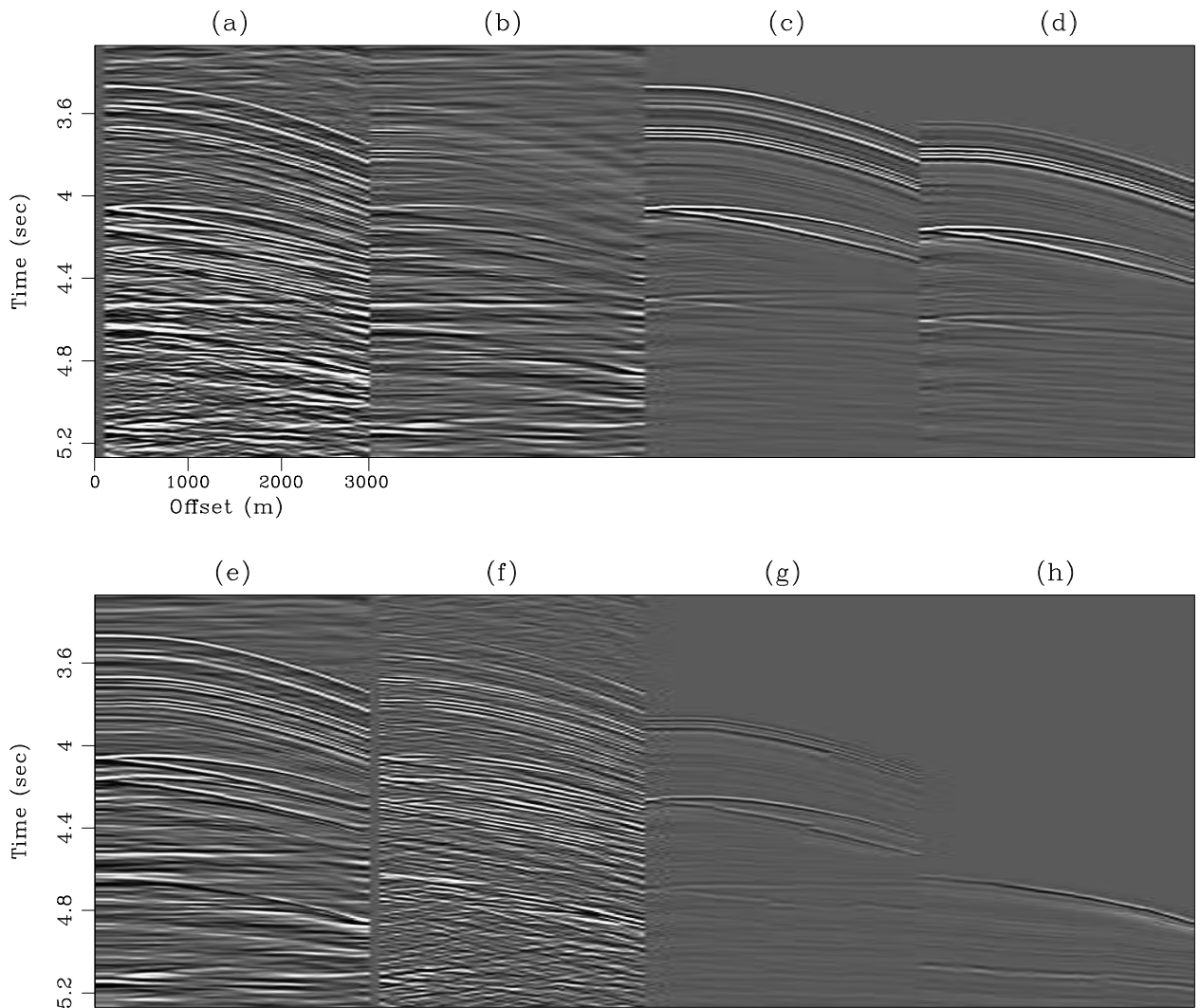


Figure 3.10: Mississippi Canyon CMP 344 (9150 m). Events labeled as in Figure 3.1. All panels NMO'ed with stacking velocity and windowed in time from 3.5 to 5.5 seconds and gained with t^2 . (a) Raw data; (b) Estimated primaries (\mathbf{m}_0); (c) Estimated WB peglegs; (d) Estimated R1 peglegs; (e) Estimated data (sum of (b), (c), (d), (g), and (h)); (f) Data residual (difference of (a) and (e)); (g) Estimated R2 peglegs; (h) Estimated TS peglegs. [results2d-comp1.4.lsrow.gulf.344](#) [CR]

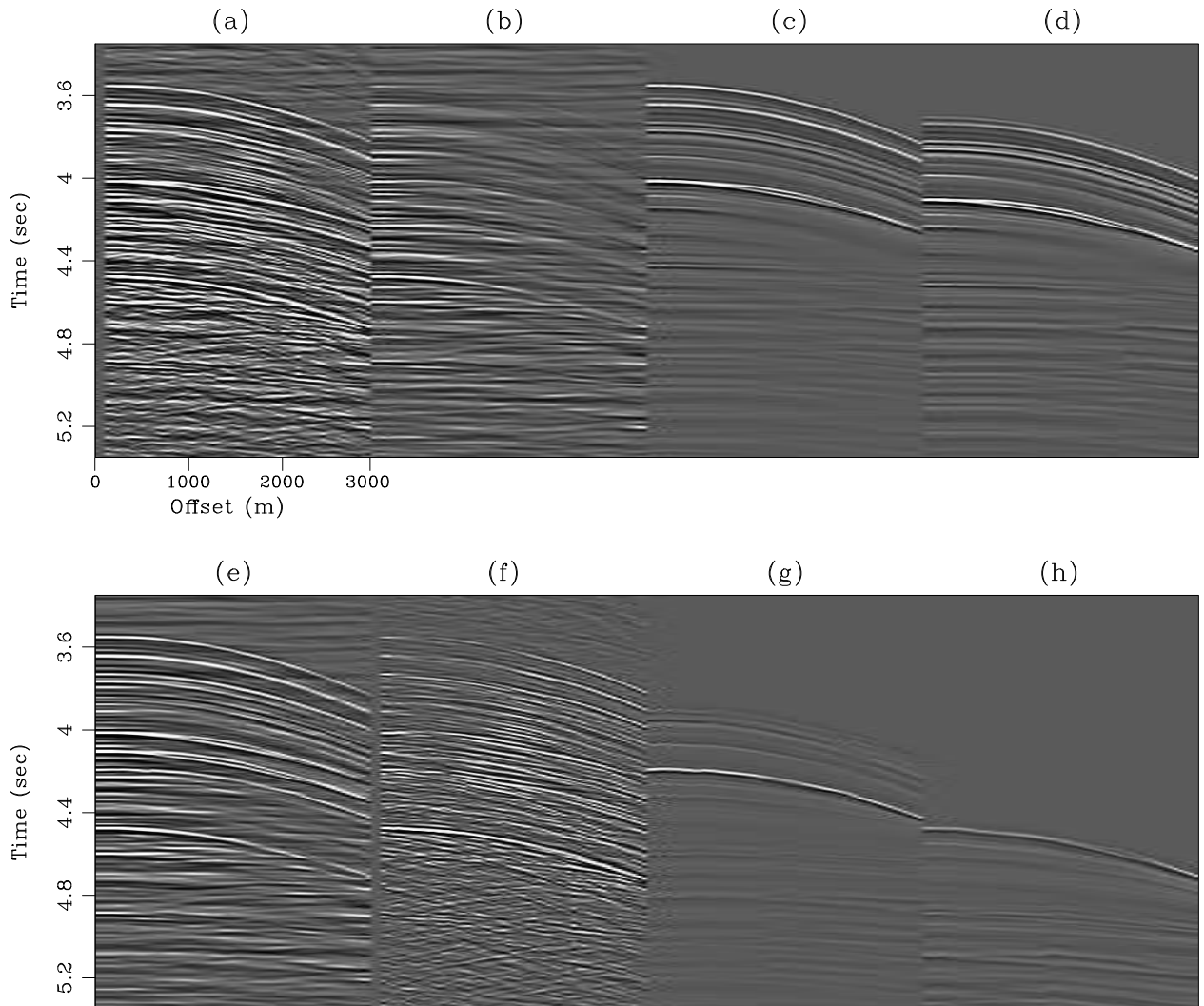


Figure 3.11: Mississippi Canyon CMP 540 (14400.0 m). Events labeled as in Figure 3.1. All panels NMO'ed with stacking velocity and windowed in time from 3.5 to 5.5 seconds and gained with t^2 . (a) Raw data; (b) Estimated primaries (\mathbf{m}_0); (c) Estimated WB peglegs; (d) Estimated R1 peglegs; (e) Estimated data (sum of (b), (c), (d), (g), and (h)); (f) Data residual (difference of (a) and (e)); (g) Estimated R2 peglegs; (h) Estimated TS peglegs. `results2d-comp1.4.lsrow.gulf.540` [CR]

3.0.1 Depth Migration Before and After LSJIMP

My particular LSJIMP implementation would likely come early in a modern seismic processing flow; after stacking velocity analysis, but before depth migration and interval velocity model building. Therefore a scenario of considerable practical interest is to view LSJIMP as a multiple suppression algorithm, and to treat the estimated LSJIMP primaries (after inverse NMO) as demultiplied data, which would then be depth migrated.

WesternGeco supplied a depth interval velocity model with the data. I migrated the raw data and the LSJIMP primary data using a 2-D Extended Split-Step prestack depth migration algorithm (Stoffa et al., 1990) with three so-called “reference velocities” to handle lateral velocity variation. Image sampling in depth is 6.67 meters. The migration algorithm outputs gathers as a function of depth, midpoint, and subsurface offset. Using the method of Sava and Fomel (2000), the offset gathers are converted to Angle-domain Common-image gathers (ADCIGs) as a function of opening angle at the reflector.

Figure 3.12 shows angle stacks, after a $z^{1.5}$ gain, of the Mississippi Canyon raw data, the data after LSJIMP, and the difference of the two. The Figure is similar in style to Figure 3.6. The removed multiples are simplest to view on the left-hand side of the section, where the geology is less complicated than under the salt body. In the sedimentary region, we notice, as before, that LSJIMP can cleanly separate primaries from many different multiple reflections. In the salt region, the results are somewhat muddled, since migration strongly defocuses multiples. We see that much multiple energy has been removed, though much remains. Subsalt primaries, already difficult to spot without any multiple energy, are uncovered better, especially around 3500 meters depth. The dominant dip is negative (toward the surface with increasing midpoint).

For reasons explained in more detail in section 3.0.2, some primary energy is seen on the difference panel, where we hope to see only multiple energy. The loss of primary energy, while well below the clip value anywhere, is strongest for the top of salt reflection. Much of the lost energy has a high spatial wavenumber, and likely arises from diffractions which my implementation of LSJIMP cannot model. Also, the large velocity contrast at the top of salt gives rise to strong head waves, which have a high apparent velocity. These events, which are

not flat after NMO for primaries, are filtered out as noise by the LSJIMP regularization which differences across offset.

Figures 3.13 and 3.14 illustrate, after $z^{1.5}$ gain, ADCIGs at midpoints 55 and 344 (of 750), respectively. Compare these Figures to Figures 3.9 and 3.10. Figure 3.13 is extracted from the sedimentary region of the data. Notice that LSJIMP has quite cleanly separated multiples from the primaries, and certainly improved our ability to interpret the angle gather for amplitude-versus-angle phenomena.

Figure 3.14, on the other hand, is extracted from the salt-bearing region of the data. Visually, it is far more difficult on the angle gather to distinguish primaries from multiples, although peglegs from shallow reflectors, between 3500 and 4300 meters depth, are recognizable and cleanly removed from the data, uncovering some hidden primaries. Notice that some downcurving reflections within the salt (1900 to 2800 meters depth), which may be internal multiples, are attenuated by LSJIMP, since they are not flat like true signal events. Furthermore, the events with negative dip below 4000 meters, which may be out-of-plane reflections or diffractions, are also attenuated somewhat.

3.0.2 A closer look at the residuals

The theoretical development of the LSJIMP algorithm given in Chapter 2 defines the data and model residuals in mathematical and algorithmic terms, but in this section, I more practically illustrate the structure of and relationship between the residual vectors with a real data example. Figures 3.15-3.20 were computed at CMP 55 or 750 of the Mississippi Canyon 2-D dataset, in the sedimentary region of the data. Figures which display seismic data are divided in half along the time axis and clipped independently for viewing purposes.

Figure 3.15 illustrates, as a function of conjugate gradient iteration, the norm of the data and model residuals from the LSJIMP inversion at CMP 55. Although the norm of the combined model and data residual [equation (2.12)] is guaranteed to decrease with iteration, we see that the individual residuals may decrease at different rates, or even increase with iteration. Of particular interest in the Figure is the model residual corresponding to differentiation across

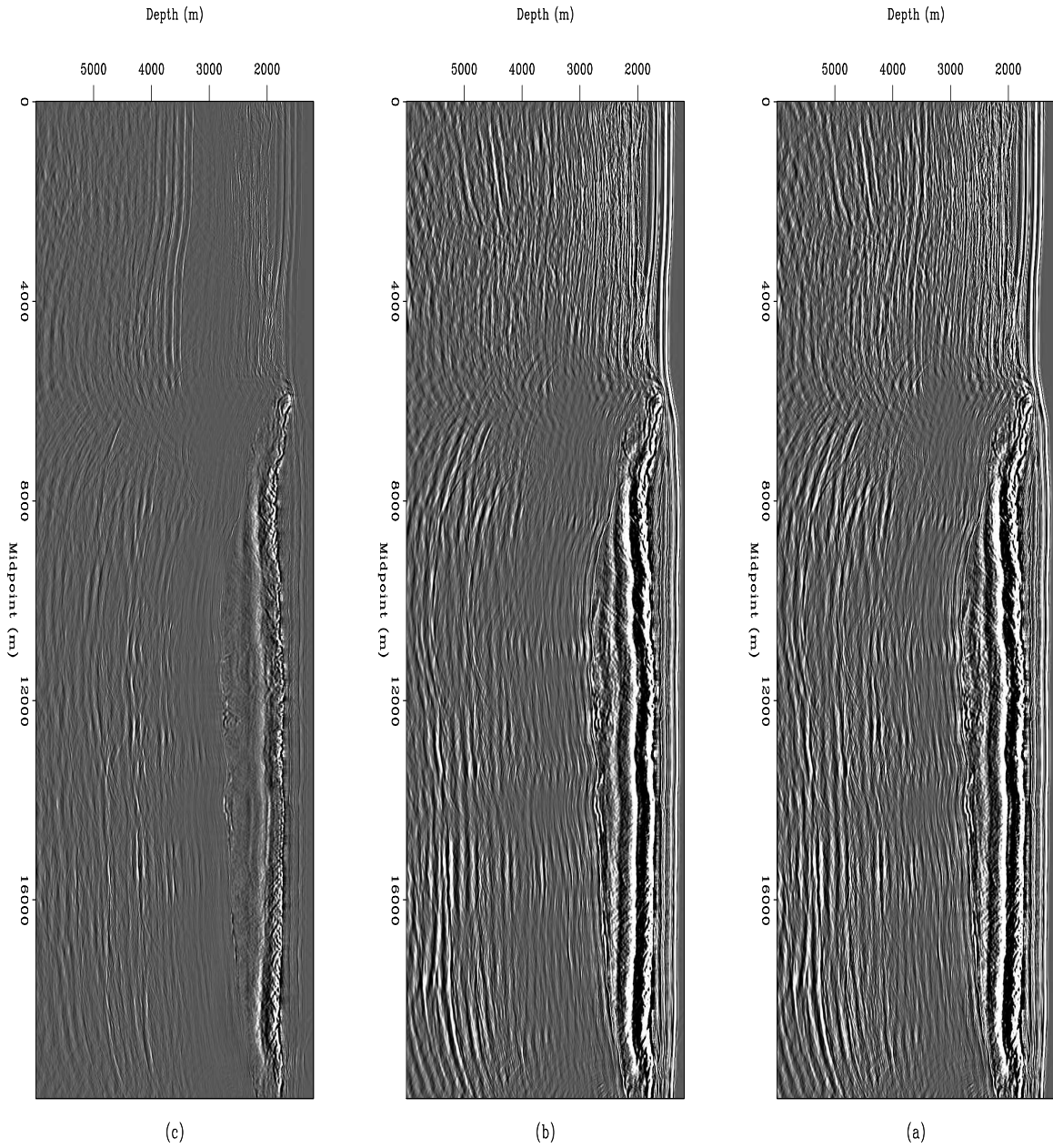


Figure 3.12: Angle stacks after prestack depth migration. Panel (a): Raw data. Panel (b): LSJIMP estimated primaries after inverse NMO. Panel (c): Difference. [results2d-stackcomp-weimig.gulf](#) [CR,M]

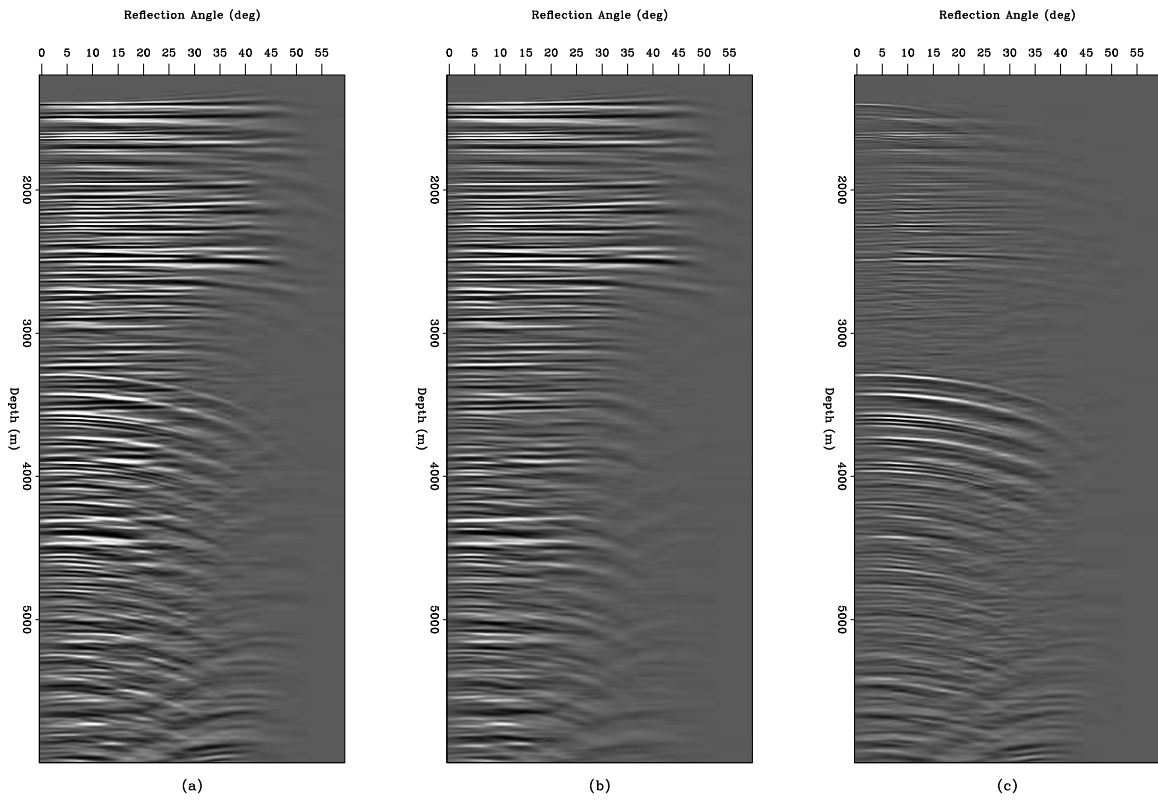


Figure 3.13: Angle gather comparison at CMP 55 of 750. Panel (a): Raw data. Panel (b): LSJIMP estimated primaries after inverse NMO. Panel (c): Difference. [results2d-angcomp.weimig.gulf.55](#) [CR]

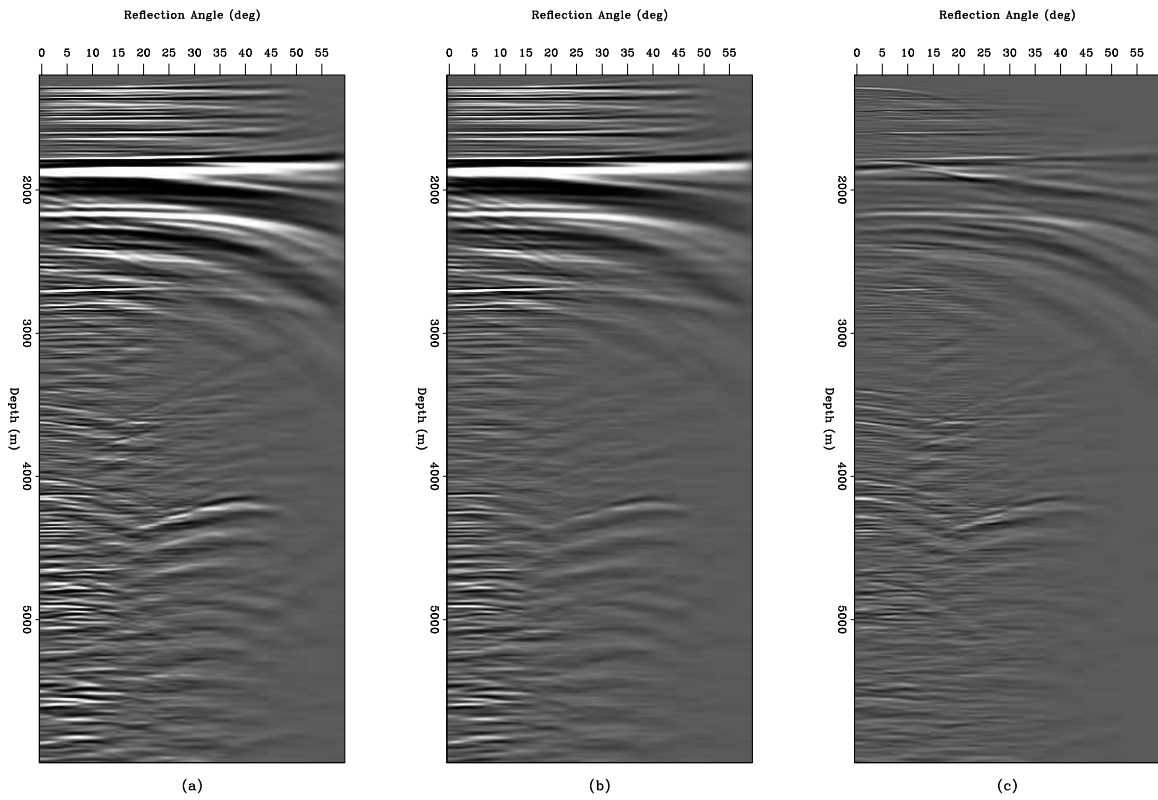


Figure 3.14: Angle gather comparison at CMP 344 of 750. Panel (a): Raw data. Panel (b): LSJIMP estimated primaries after inverse NMO. Panel (c): Difference. [results2d-angcomp.weimig.gulf.344](#) [CR]

individual images ($\mathbf{r}_m^{[1]}$ in equation (2.12)). As a starting guess, I simply “spread” a stacked trace of the primaries across all offsets, for all images. $\mathbf{r}_m^{[1]}$ is roughly a measure of image dissimilarity. As the images are adjusted to fit variations in the data, the images become more dissimilar, and the model residual initially increases, before decreasing slowly with iteration.

Figure 3.15: Individual data and model residuals as a function of iteration for LSJIMP inversion, CMP 55 of 750. “rm_ord”, “rm_off”, and “rm_xtalk” derive from $\mathbf{r}_m^{[1]}$, $\mathbf{r}_m^{[2]}$, and $\mathbf{r}_m^{[3]}$ in equation (2.12), respectively, while “rm_tot” is the sum of these residuals. “rd” is the data residual, while “total” denotes the combined LSJIMP residual of equation (2.12).

[results2d-respaw.gulf](#) [CR]

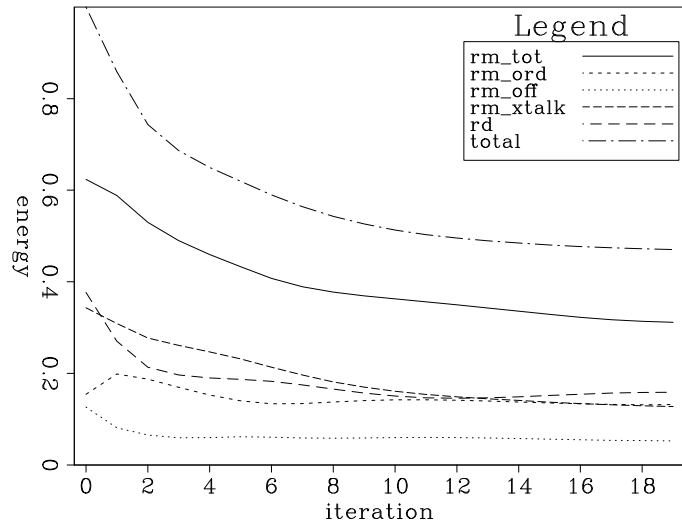


Figure 3.16 compares the data residual and raw data at CMP 55. A somewhat similar comparison was made earlier, in Figures 3.9-3.11, to examine the quality of fit to the multiples, but the earlier portions of the time axis were not shown. At earlier times, notice that the data residual contains some primary energy. The model regularization terms in the LSJIMP inversion cause the misfit. LSJIMP’s working definition of “signal” includes events that are perfectly flat with offset on all images (with “smooth” AVO variation) and perfectly self-consistent multiple and primary images. If, for instance, the stacking velocity does not perfectly flatten a primary, or if primary and multiple events are misaligned or mis-modeled in terms of amplitude, we will see some primary energy in the data residual. Furthermore, notice increased misfit at near offsets versus far offsets. As noted in Section 2.2, the model regularization operators are not applied where the multiples provide no information – specifically, as far offsets, as dictated by Snell Resampling. The fact that we see little to no residual primary energy at far offsets confirms the notion that model regularization terms cause the observed misfit at near offsets.

Figure 3.17 simply shows all nine (four multiple generators, first-order multiples only) panels of the model space at CMP 55. Comparing the primary image (“m0”) directly with the

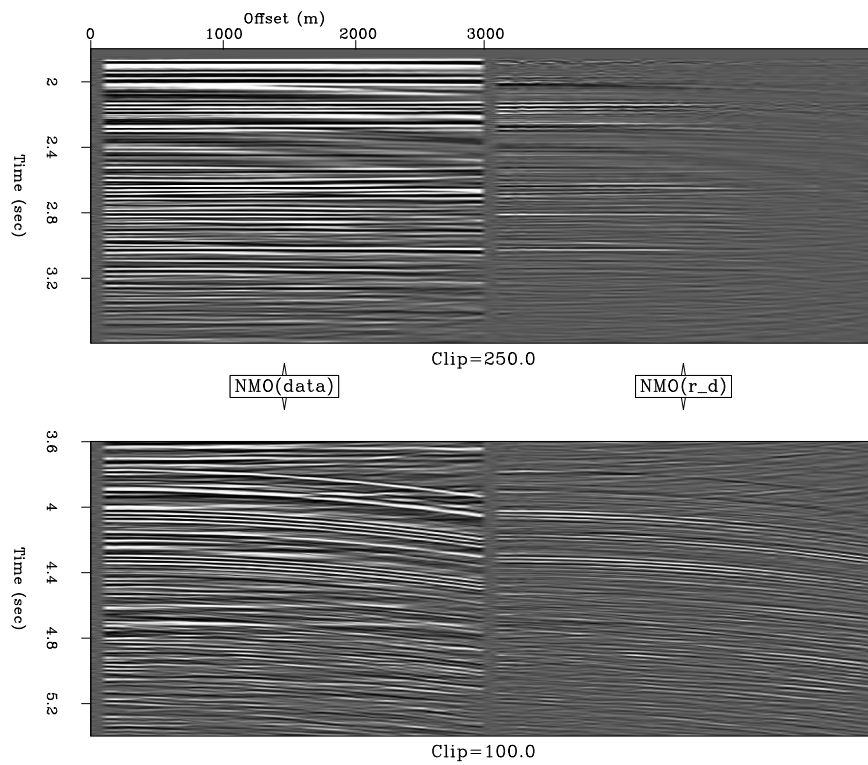


Figure 3.16: Raw data (left) and data residual (right) compared for CMP 55 of 750. NMO with primary stacking velocity applied to facilitate discrimination between multiples and primaries. `results2d-resd.gulf` [CR]

raw data shown in Figure 3.16, notice that obvious multiples have been strongly, but not totally, suppressed and that two prominent primary reflections between 4.4 and 4.8 seconds uncovered. This Figure and Figures 3.18-3.20, which display the various model residual vectors, have the same graphical layout.

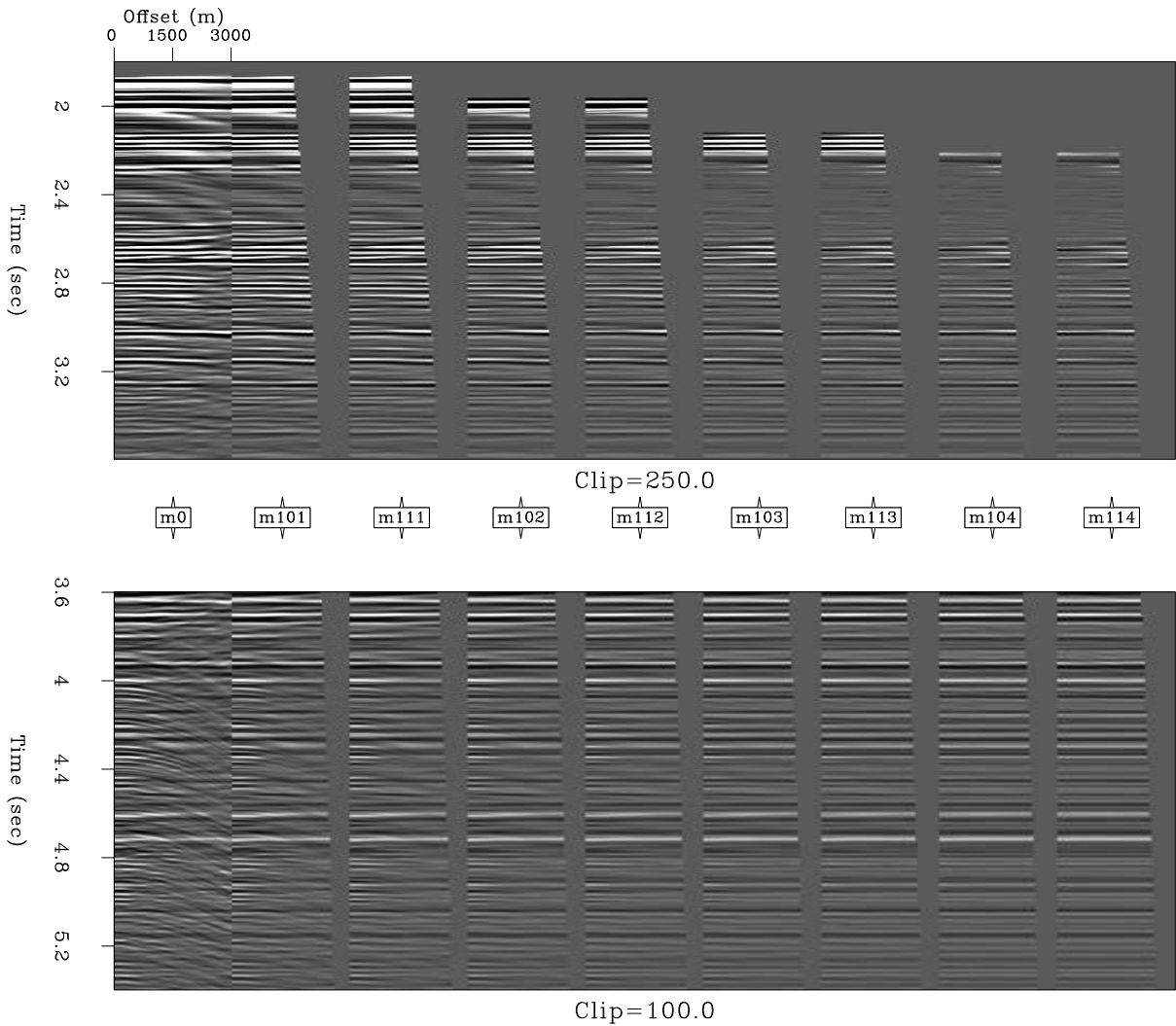


Figure 3.17: LSJIMP model space at CMP 55 of 750. “m0” is the primary image, \mathbf{m}_0 , while “mikm” corresponds to $\mathbf{m}_{i,k,m}$, the image of the k^{th} split of the i^{th} -order pegleg multiple from the m^{th} multiple generator. [results2d-model.gulf](#) [CR]

Figure 3.18 illustrates the model residual corresponding to the differencing across images

regularization operator derived in Section 2.1.4, and to $\mathbf{r}_m^{[1]}$ in equation (2.12). First notice that the last panel, “m114” is blank. The differencing operator subtracts one image panel from the previous, in exactly the left-to-right order shown on the Figure. The difference is not defined for the last image, here “m114”. The difference is zero-valued at far offsets, because the multiples provide no information here, as mentioned in the discussion of Figure 3.16. Above the onset of the seabed pure multiple, notice on the residual panels some primary energy, the presence of which can be explained by misalignment of primaries and multiples after imaging or by inaccuracies in the amplitude modeling of the multiples. In theory, after proper imaging, the multiples should be “copies of the primary”; any deviations from this state will appear on the model residual shown in Figure 3.18. At later times, we notice considerable residual multiple energy. As discussed in Section 2.1.4 (Figure 2.1), crosstalk events from one image panel to another do not generally coincide at far offsets.

Figure 3.18 illustrates the model residual corresponding to the differencing across offset regularization operator derived in Section 2.1.5, and to $\mathbf{r}_m^{[2]}$ in equation (2.12). The panels are fairly simple to understand; the differencing filter amplifies high spatial wavenumber events, such as multiples at far offsets, random noise, or non-flat primaries. Notice that the difference is not taken at the far offsets of the multiple panels, where no multiple energy is recorded.

Figure 3.20 illustrates the model residual corresponding to the crosstalk penalty weighting regularization operator derived in Section 2.1.6, and to $\mathbf{r}_m^{[3]}$ in equation (2.12). Conceptually, the panels are easily understood; each is simply the result of applying the crosstalk weight to the corresponding panel of the LSJIMP estimated model (Figure 3.17). In the case of the primary panel, “m0”, the weight attempts to penalize all the modeled multiples. In the case of the multiple panels, the weight attempts to penalize multiples from all the other multiple generators.

3.1 SRME versus HEMNO

Verschuur et al. (1992) of Delft University presented a very effective autoconvolutional modeling technique for surface-related multiples, known as the “SRME” (Surface-related Multiple Elimination) method. Assuming sufficiently dense source coverage, as is typical with 2-D

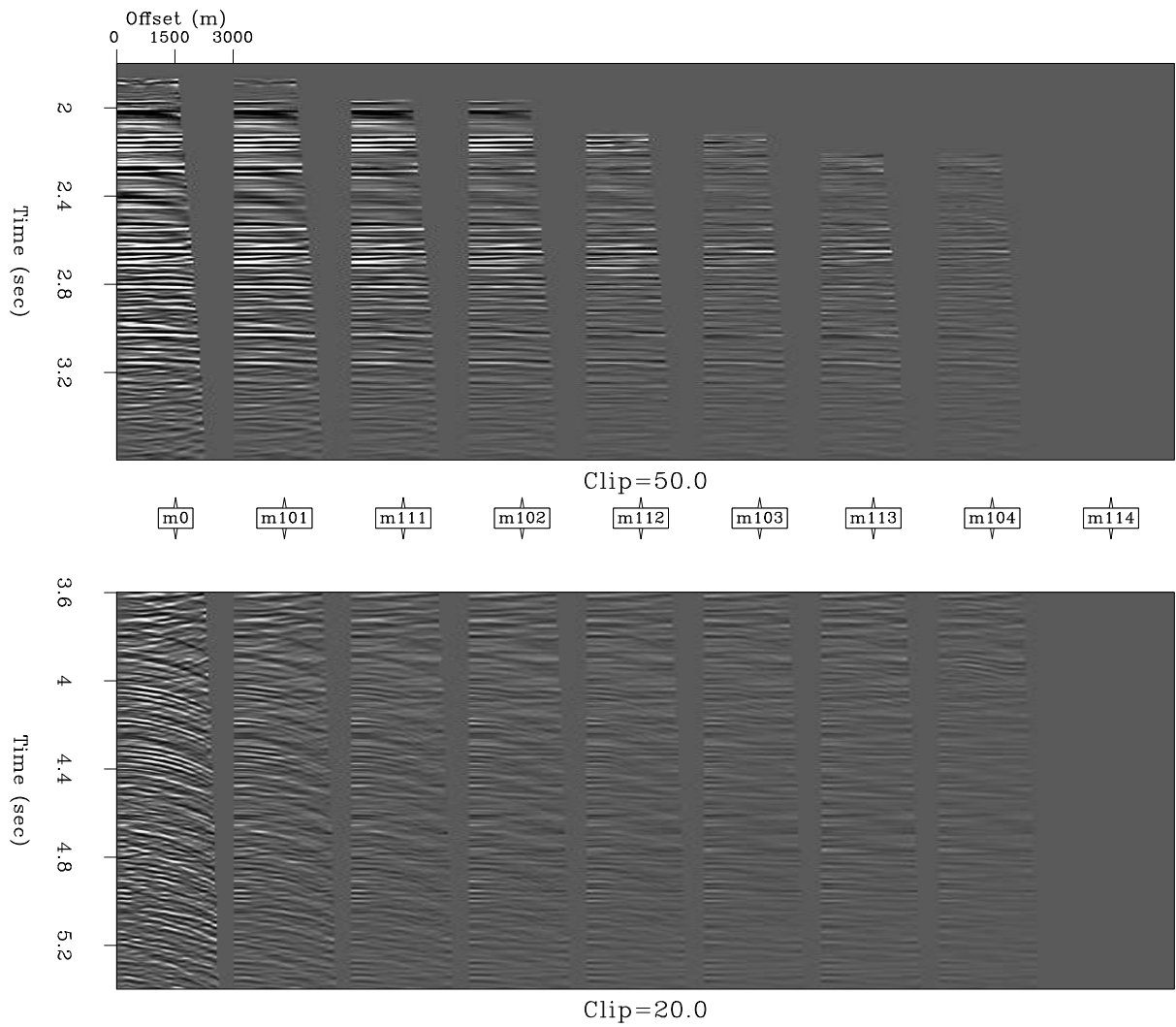


Figure 3.18: LSJIMP model residual $\mathbf{r}_m^{[1]}$ at CMP 55 of 750. Each panel is the difference of one panel of the estimated model and the next panel to the right (see Figure 3.17). [results2d-resm.order.gulf](#) [CR]

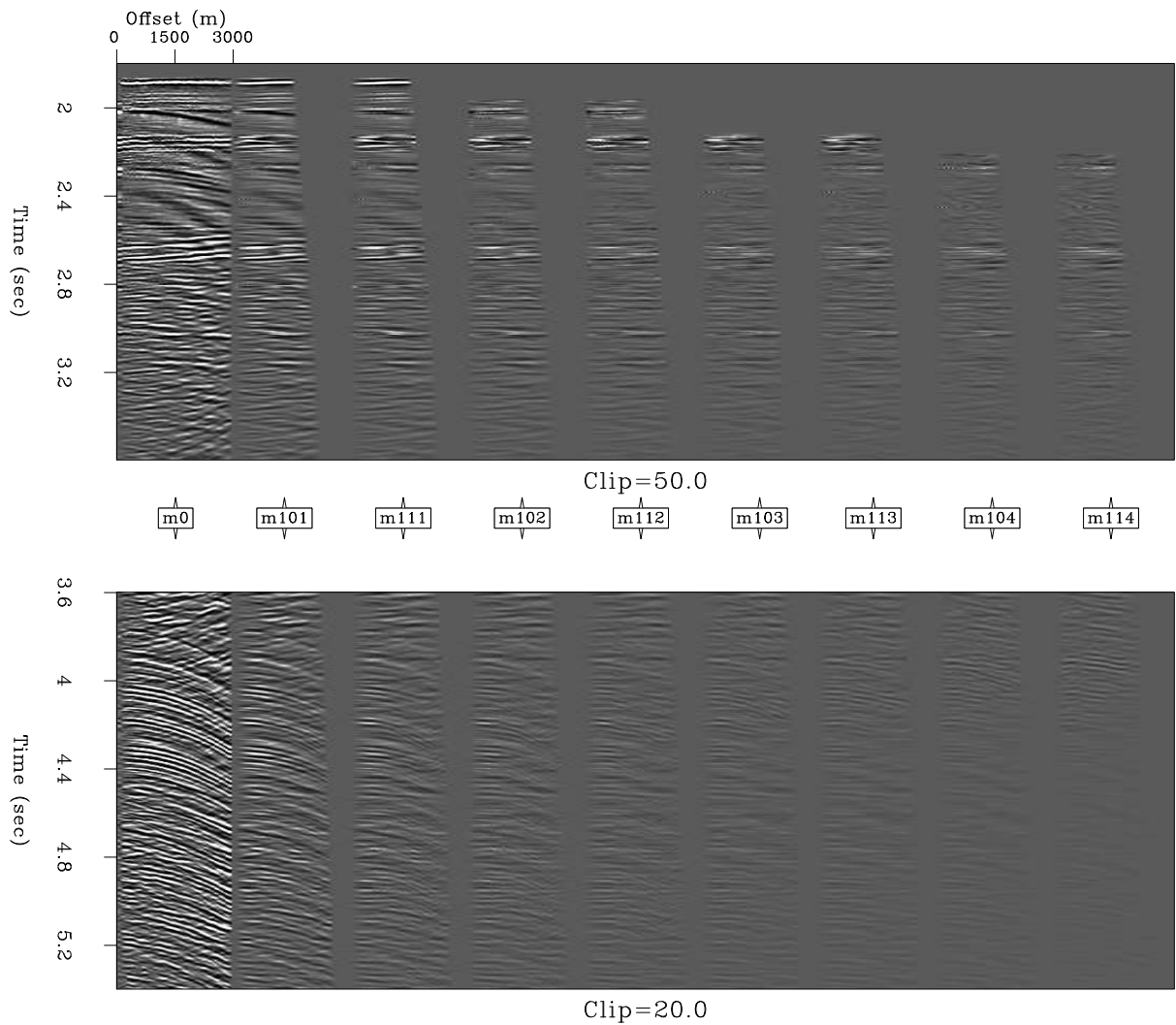


Figure 3.19: LSJIMP model residual $\mathbf{r}_m^{[2]}$ at CMP 55 of 750. Each sample of each panel is the difference of that sample and the adjacent sample in offset, on the corresponding estimated model panel (see Figure 3.17). `results2d-resm.offsetx.gulf` [CR]

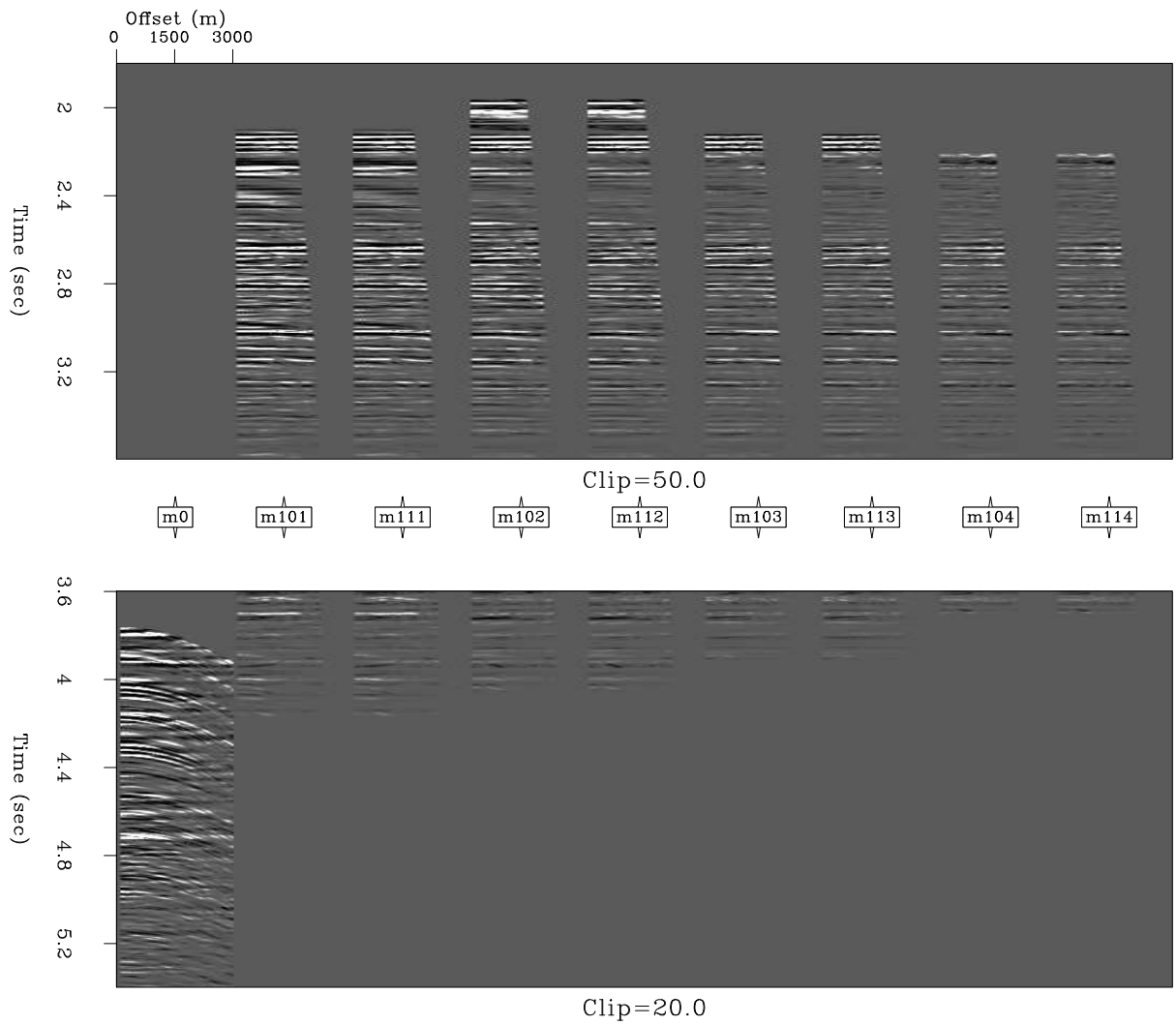


Figure 3.20: LSJIMP model residual $\mathbf{r}_m^{[3]}$ at CMP 55 of 750. Each panel is the result of applying crosstalk weights to the corresponding estimated model panel (see Figure 3.17). `results2d-resm.xtalk.gulf` [CR]

towed-streamer marine data, the method accurately models all multiples which bounce downward at the acquisition datum, but nowhere else. SRME can model diffracted multiples and other complex events, and most compellingly, requires no prior knowledge of the subsurface geology. Once estimated, the SRME multiple model is usually subtracted from the recorded data by any number of adaptive subtraction techniques.

Postponing a discussion of SRME's limitations with 3-D narrow azimuth marine data until Chapter 4, the method has a number of limitations in 2-D. The method obtains a multiple model by iteratively adding terms of an infinite series, although in practice only one iteration is done. After one iteration, the wavelet of the multiple model will generally be stretched somewhat because it is generated via autoconvolution. Additionally, the near-offset gap of the multiple model is twice that in the data. Since near-offset multiple energy contributes most to the stack, accurate extrapolation of the near-offset traces is crucial. Another limitation of SRME is its tendency to "over-predict" higher-order multiples; this may hamper some subtraction algorithms.

In this section, I compare an SRME multiple model (one iteration), computed by Antoine Guitton, with a multiple model generated by the method outlined previously for the computation of crosstalk (section 2.1.6), using HEMNO as the imaging engine. Figures 3.21 and 3.22 compare the SRME and HEMNO results at CMP locations 55 (1440 m) and 344 (9150 m), respectively. The results of LSJIMP at same CMP locations are shown in Figures 3.9 and 3.10.

Figure 3.21 is taken from the sedimentary basin portion of the Mississippi Canyon data. We first notice the improved near-offset coverage of the HEMNO model. Kinematically, both HEMNO and SRME match the shallow multiple events quite accurately. Deeper in the gather, we see little order to the multiples in the data. Many of the primaries in the 2.5-3.5 second range may come from out-of-plane reflectors or diffractors, hence the multiples of these events will not have the expected kinematics. In 2-D, both HEMNO and SRME assume that all energy propagates in the plane of acquisition. Figure 3.22 is taken from over the salt body. Notice that both the HEMNO and SRME models fairly accurately represent the strong split peglegs from the top of salt reflection.

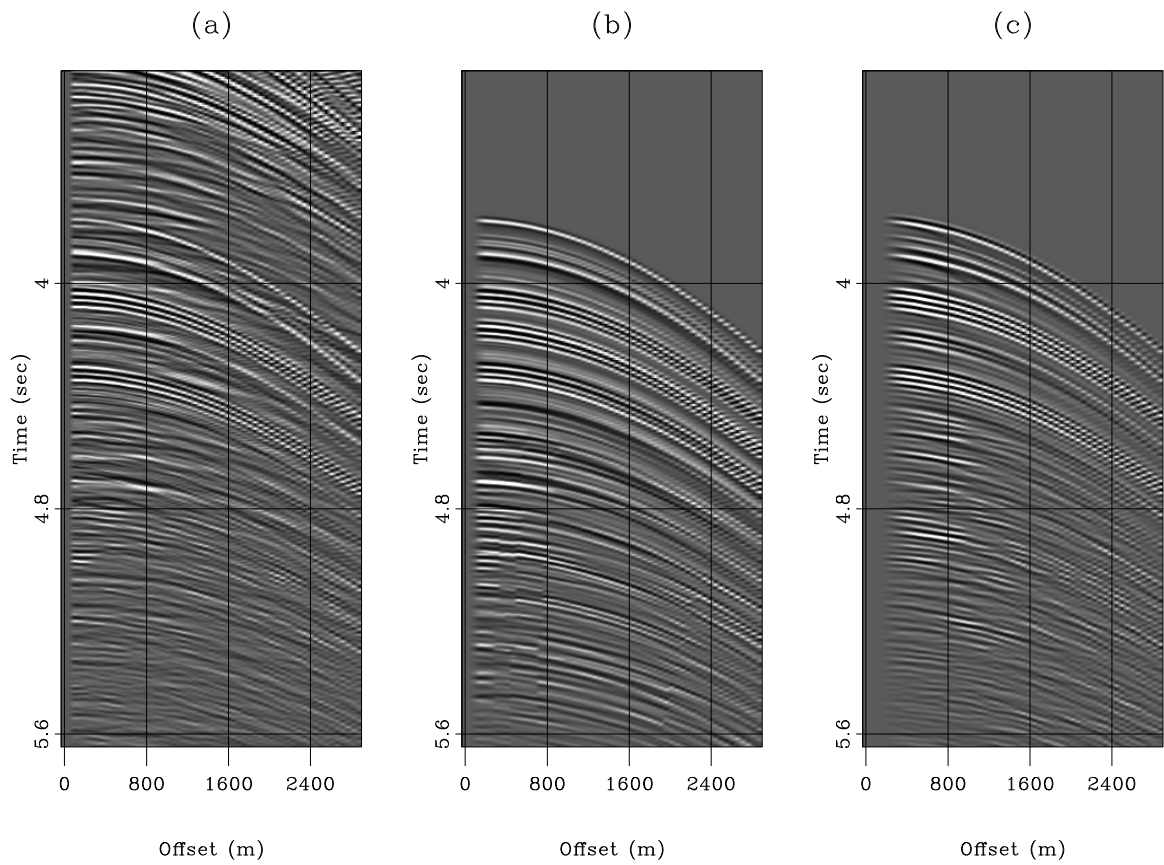


Figure 3.21: HEMNO versus SRME comparison, CMP 55 (1440m). Left: raw data. Center: HEMNO multiple model. Right: SRME multiple model. [results2d-delft.comp.55](#) [CR]

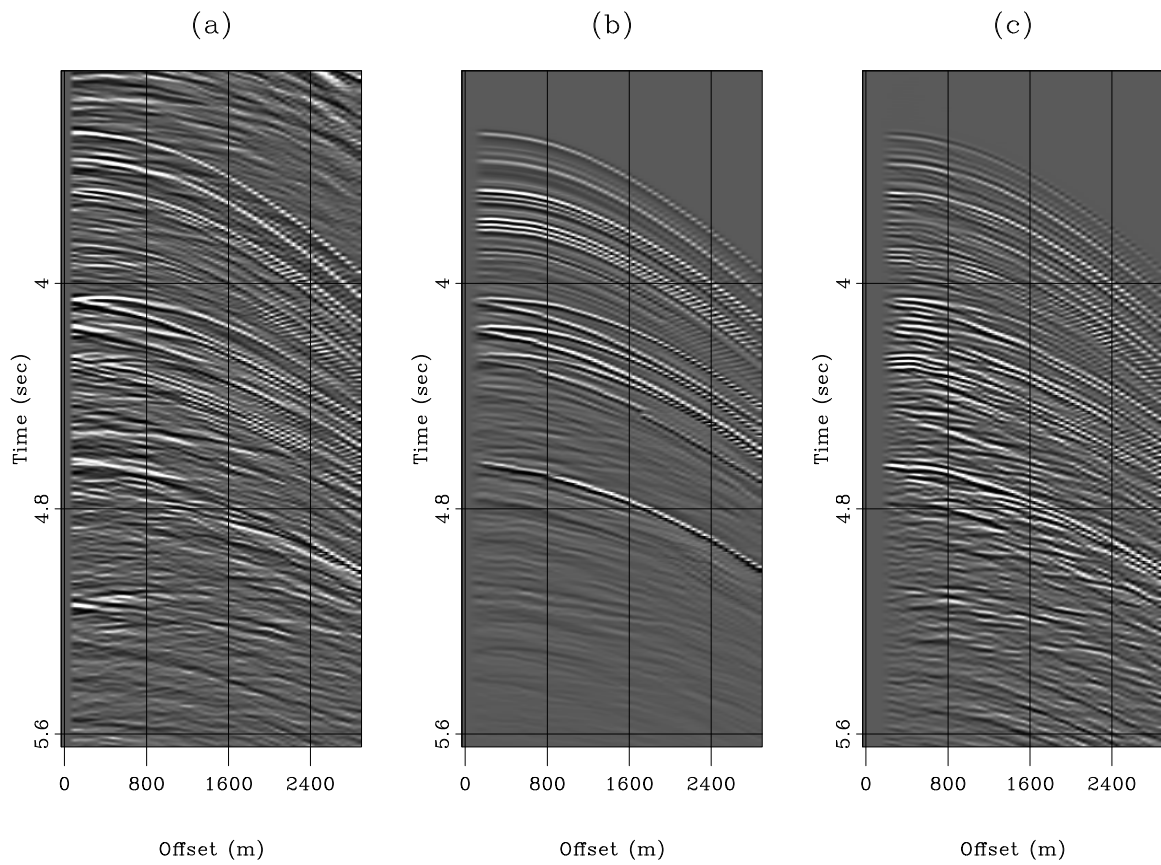


Figure 3.22: HEMNO versus SRME comparison, CMP 344 (9150). Left: raw data. Center: HEMNO multiple model. Right: SRME multiple model. `results2d-delft.comp.344` [CR]

Figures 3.23 and 3.24 compare the HEMNO and SRME multiple models on constant-offset sections. Here, we can check each model for correct event positioning—especially important when complex peglegs split. On a near-offset section (Figure 3.23), we see that both methods accurately match the kinematics of the important multiple reflections. The region highlighted by the circle illustrates the stretched wavelet of the SRME model. The region highlighted by the oval shows how the poorly-estimated R1 reflection coefficient has caused an overly strong event to appear in the HEMNO model. On a medium-offset section (Figure 3.24) we again see that both models roughly mimic the multiples in the data. Of special interest is the positioning of split multiple events. In the region highlighted by the circle, all three methods correctly model the split pegleg. The amplitudes on the HEMNO model appear truer to the data. In the region highlighted by the tall oval, we see that the HEMNO model does not accurately represent the data, but the SRME model does. In the region highlighted by the wide oval, we see that SRME better models the diffractions and other features of the complex top of salt pure multiple.

3.2 Playing Devil’s Advocate: What do the multiples add?

LSJIMP seeks to exploit another type of multiplicity in the data, that between multiples and primaries. I claimed in Chapter 2 that by adding the model regularization which differences between images (section 2.1.5), we expect that information from the multiples can fill illumination holes or missing trace and also lead to better discrimination between signal and noise. The veracity of this claim is central to the labeling of LSJIMP as a “joint imaging” algorithm. If false, then we conclude that the multiples add nothing to the inversion. I ran a simple test to determine what, if anything, the multiples add to the LSJIMP inversion, I “turn off” the regularization which differences across images by setting $\epsilon_2 = 0$ in equation (2.12). Figures 3.25-3.28 show the results of this test.

Figure 3.25 shows the stack of the estimated primaries, \mathbf{m}_0 , with $\epsilon_2 = 0$, and can be compared directly with Figure 3.6. Differences are apparent, although subtle. Generally, we notice a loss of coherency in the estimated multiples (difference panel).

More revealing are Figures 3.26 and 3.27, which show a zoomed view of two regions

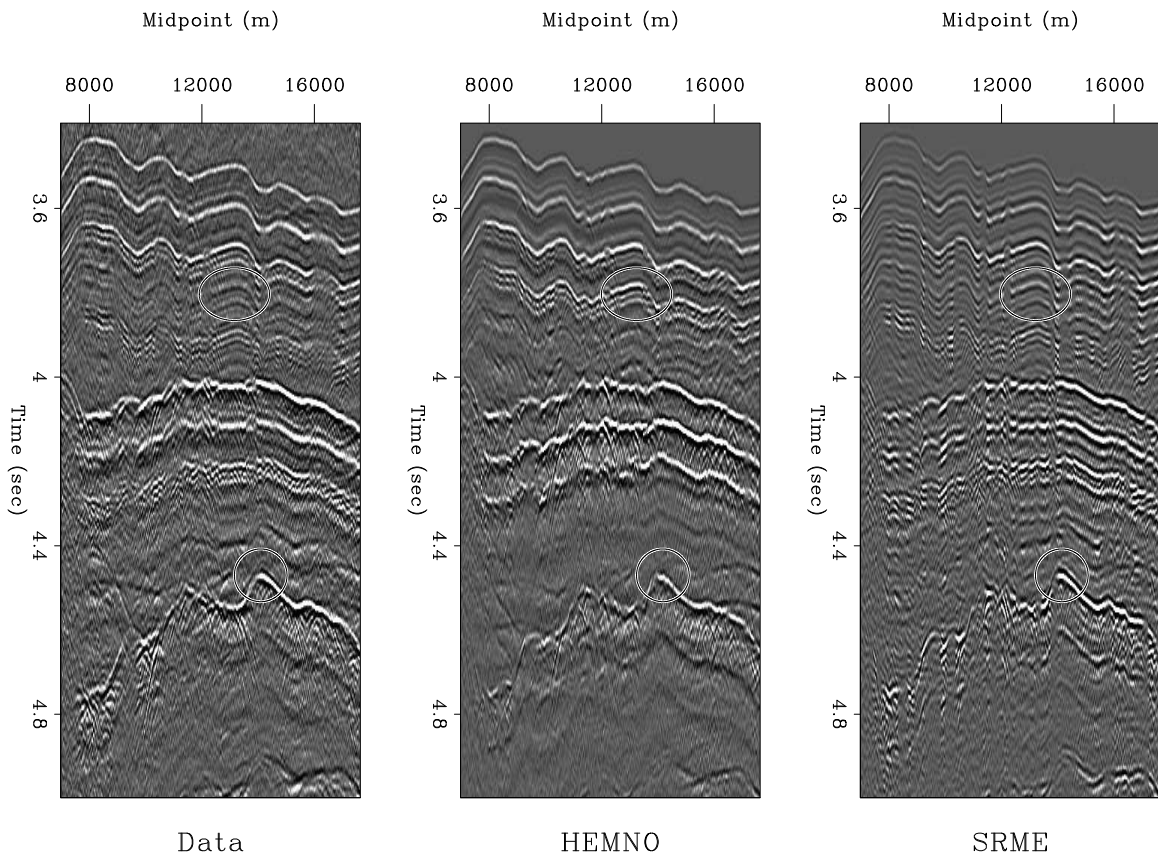


Figure 3.23: HEMNO versus SRME near-offset comparison. Left: raw data. Center: HEMNO multiple model. Right: SRME multiple model. Regions of interest are highlighted. `results2d-delft.noffcomp` [CR]

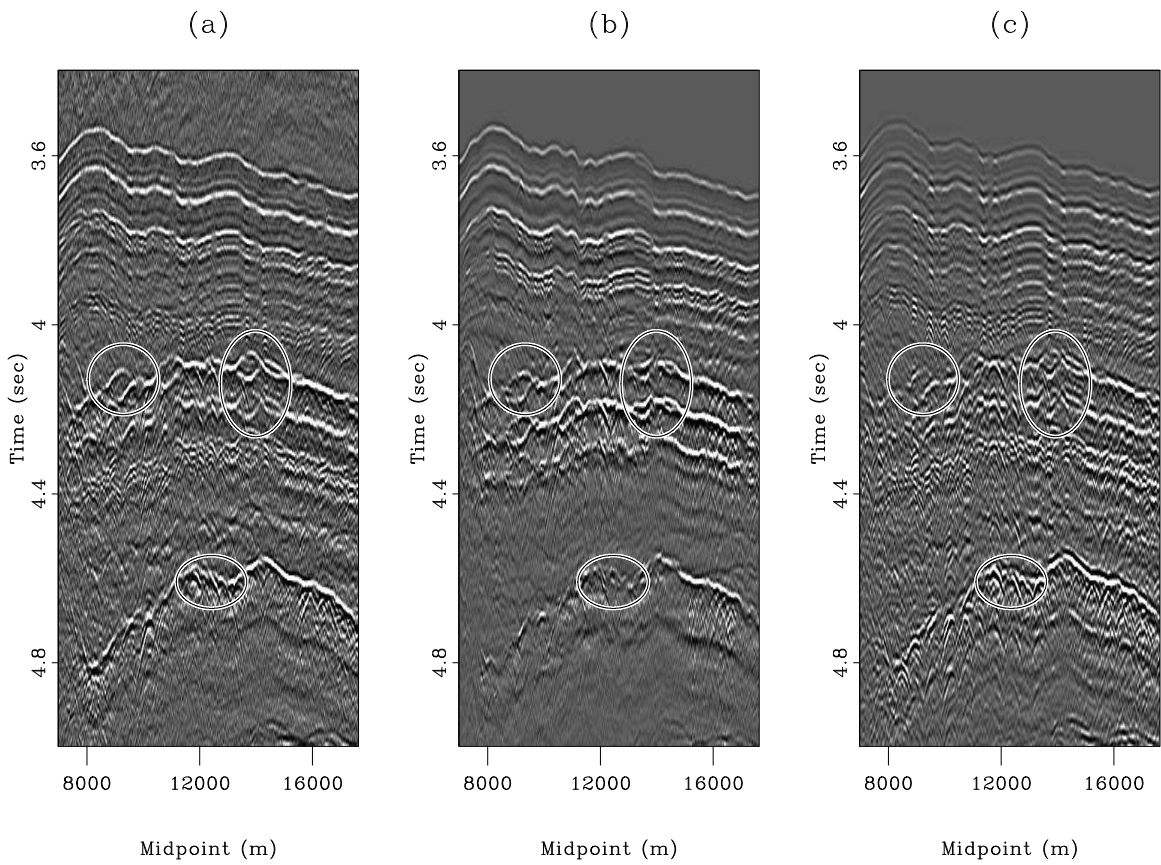


Figure 3.24: HEMNO versus SRME medium-offset comparison. Left: raw data. Center: HEMNO multiple model. Right: SRME multiple model. Regions of interest are highlighted. `results2d-delft.moffcomp` [CR]

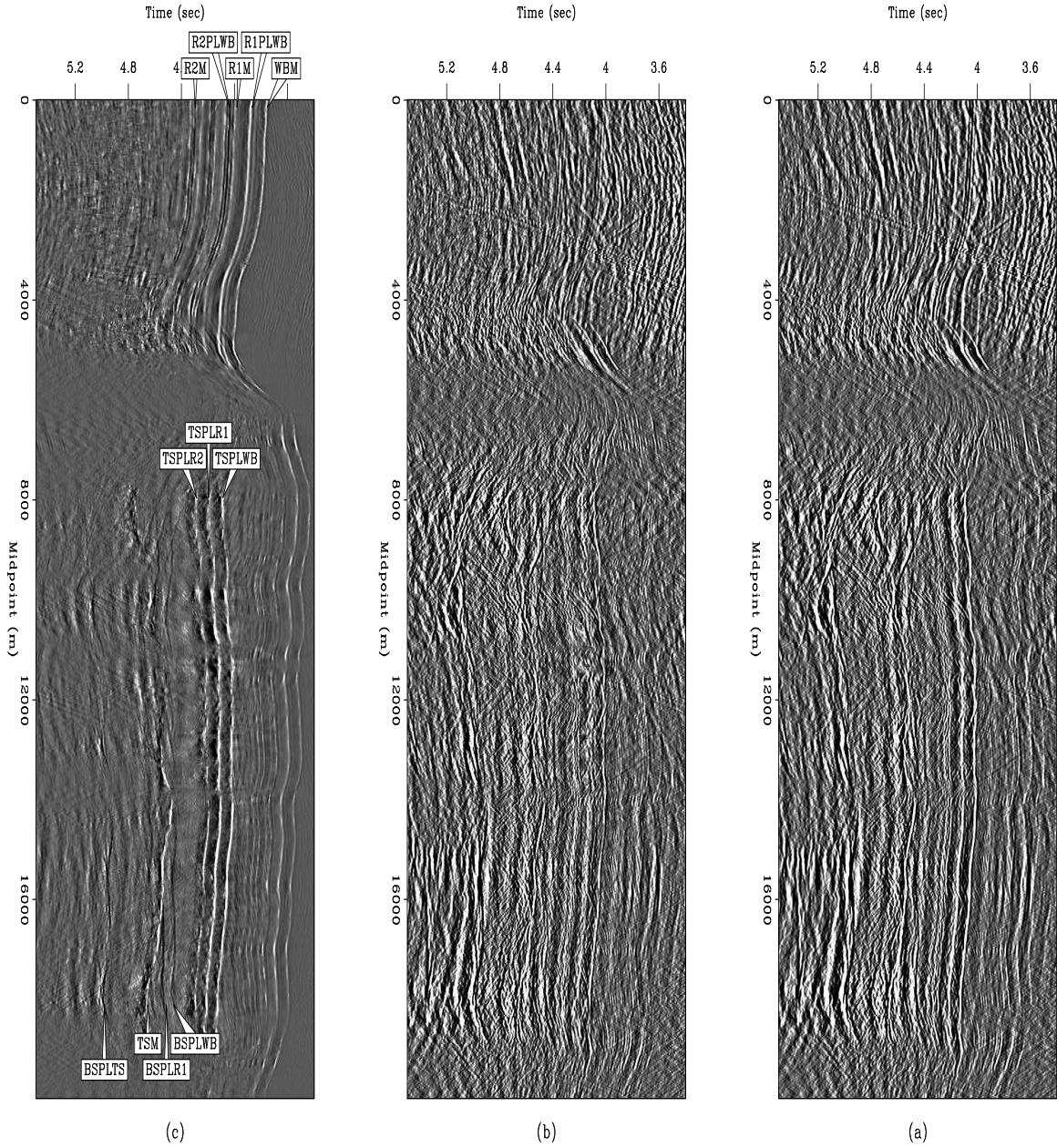


Figure 3.25: Top: raw data stack. Center: estimated LSJIMP primaries stack, with $\epsilon_2 = 0$. Bottom: difference panel (estimated multiples) stack. Compare with Figure 3.6. [results2d-stackcomp-devils.gulf](#) [CR,M]

of Figure 3.25, and are directly comparable to Figures 3.7 and 3.8, respectively. Comparing Figure 3.26 to Figure 3.7, we again note a general decrease in estimated multiple coherency when $\epsilon_2 = 0$. We also can see that in regions where multiples overlap primaries, like at 3.7 seconds/1200 meters, setting $\epsilon_2 = 0$ leads to some losses in primary energy. Comparing Figure 3.27 to Figure 3.8, we see that setting $\epsilon_2 = 0$ leads to a generally worse result. Less multiple energy is removed, particularly from some of the salt-related multiples, like TSPLWB and BSPLWB, and again, the subtracted energy is less coherent.

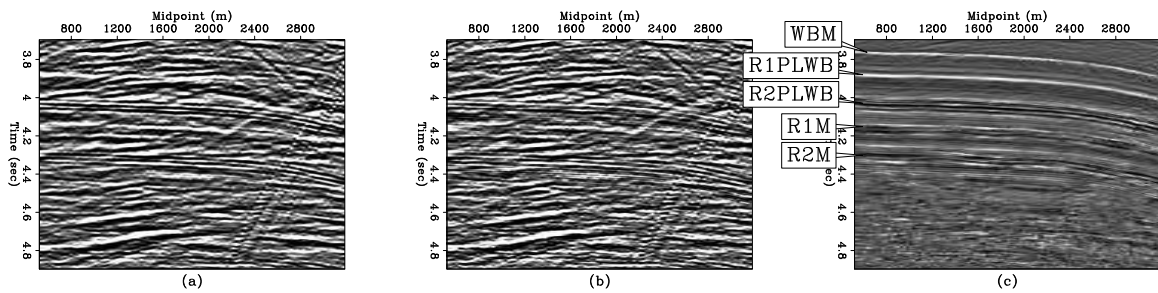


Figure 3.26: Zoom on Figure 3.25, from the sedimentary basin section of the data. Top: raw data stack. Center: estimated LSJIMP primaries stack, with $\epsilon_2 = 0$. Bottom: difference panel (estimated multiples) stack. Compare with Figure 3.7. `results2d-stackcomp-devils.zoom.1.gulf` [CR,M]

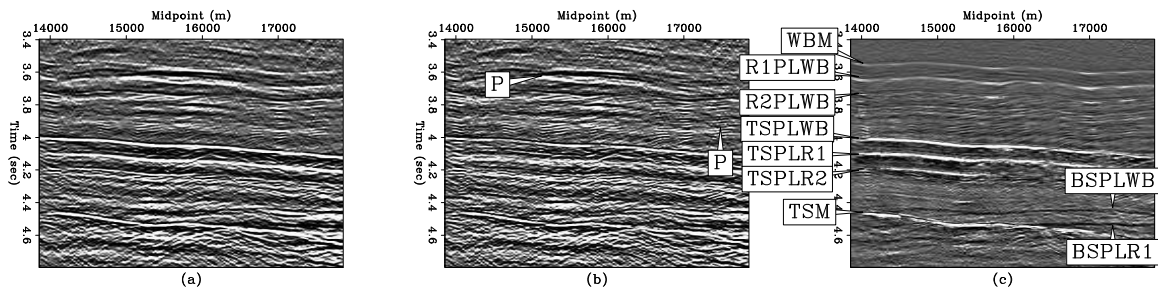


Figure 3.27: Zoom on Figure 3.25, from the subsalt section of the data. Top: raw data stack. Center: estimated LSJIMP primaries stack, with $\epsilon_2 = 0$. Bottom: difference panel (estimated multiples) stack. Compare with Figure 3.8. `results2d-stackcomp-devils.zoom.3.gulf` [CR,M]

Finally, Figure 3.28 compares the result of setting $\epsilon_2 = 0$ in the prestack sense, at CMP 55 of 750. The left-hand panels compare the estimated primaries with $\epsilon_2 = 1.0$ and $\epsilon_2 = 0$,

while the right-hand panels compare (after NMO) the data residuals for $\epsilon_2 = 1.0$ and $\epsilon_2 = 0$. The panels are split in half vertically and clipped at a different value, labeled on the plot, for display purposes. Comparing the estimated primaries, we see from the small oval that where multiples and primaries overlap, setting $\epsilon_2 = 0$ reduces the quality of the separation. Primaries are less coherent with offset, and the primary panel contains some energy corresponding to the seabed pure multiple. From the larger oval, notice that for the strongest multiples, setting $\epsilon_2 = 0$ leads to poorer separation. Comparing the data residuals, we see from the top pair of ovals that if $\epsilon_2 > 0$, we generally somewhat damage the primaries, which we expect if we have velocity errors, mis-alignment between imaged primaries and multiples, or incorrect reflection coefficient. This issue was discussed earlier, in section 3.0.2. However, we also note from the lower pair of ovals, that setting $\epsilon_2 = 0$ seems to have reduced our ability to accurately model the important multiples.

3.3 Nonlinear Iteration Test

In this section I test the nonlinear iteration outlined in section 2.1.8 on the Mississippi Canyon data. I ran only one nonlinear iteration. Since the velocity model is already quite nicely determined, I did not do residual velocity analysis after the first run of LSJIMP. However, I did recompute the crosstalk weights and the reflection coefficients for each of the four multiple generators.

The updated crosstalk weights are shown in Figure 3.29, at CMP 55 of 750. The most notable difference after the nonlinear update is the infill of the near offsets. Although invisible in this case, the nonlinear update also allows us to model crosstalk energy below twice the onset of the first seabed multiple, which would be 7.5 seconds. This ability is very important for data recorded in shallower water.

Figure 3.30 compares the weighted data residual at CMP 55 of 750 before and after the nonlinear update. The Figure is split in half along the time axis as explained earlier in section 3.0.2. The most striking differences are highlighted with ovals. As mentioned earlier, the R1 pure multiple and R2 seabed pegleg overlap over most of the 2-D line, which inhibits estimation of R1's reflection coefficient. Although I do not show the updated R1 reflection

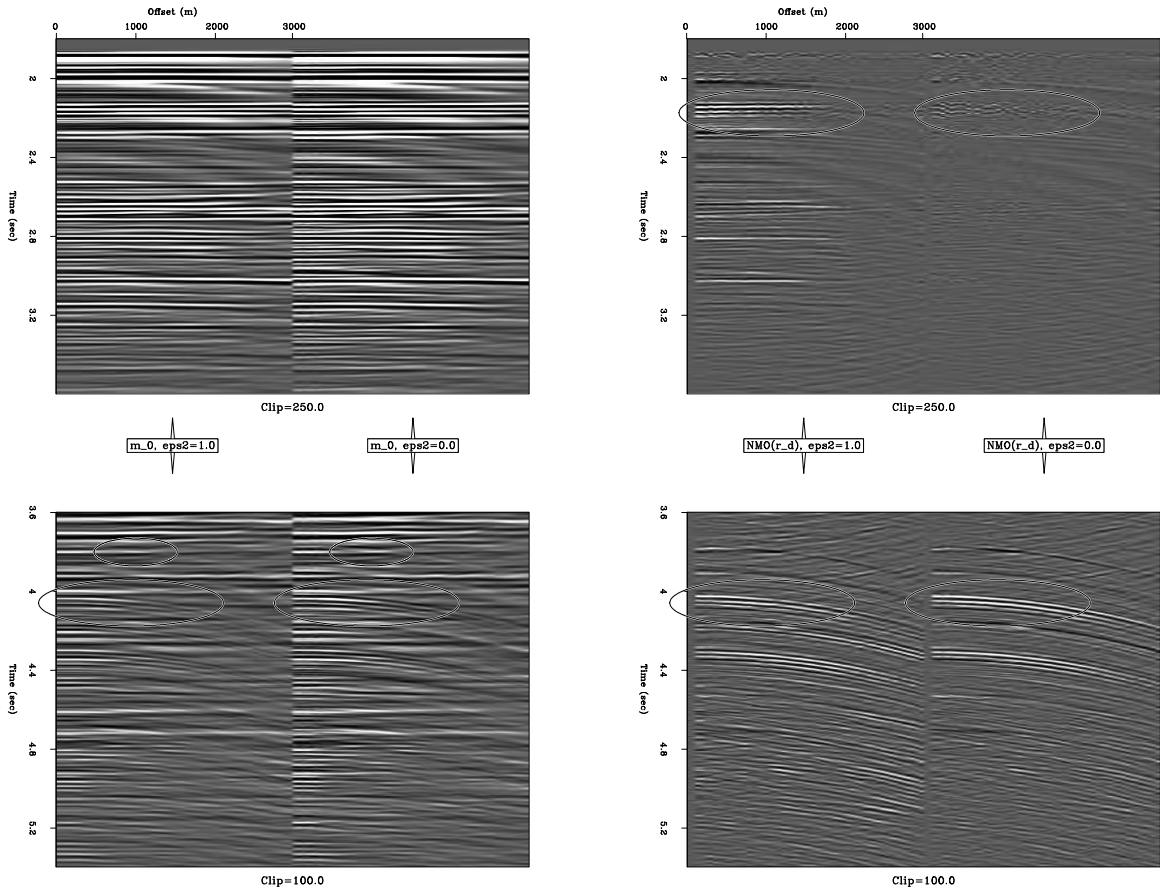


Figure 3.28: Left-hand panels: Estimated LSJIMP primaries at CMP 55 of 750, with $\epsilon_2 = 1.0$ and $\epsilon_2 = 0.0$. Right-hand panels: Weighted data residuals at CMP 55 (after NMO) with $\epsilon_2 = 1.0$ and $\epsilon_2 = 0.0$. Left-hand and right-hand panels split in half along time axis and clipped independently for display clarity. [results2d-devils.gulf](#) [CR,M]

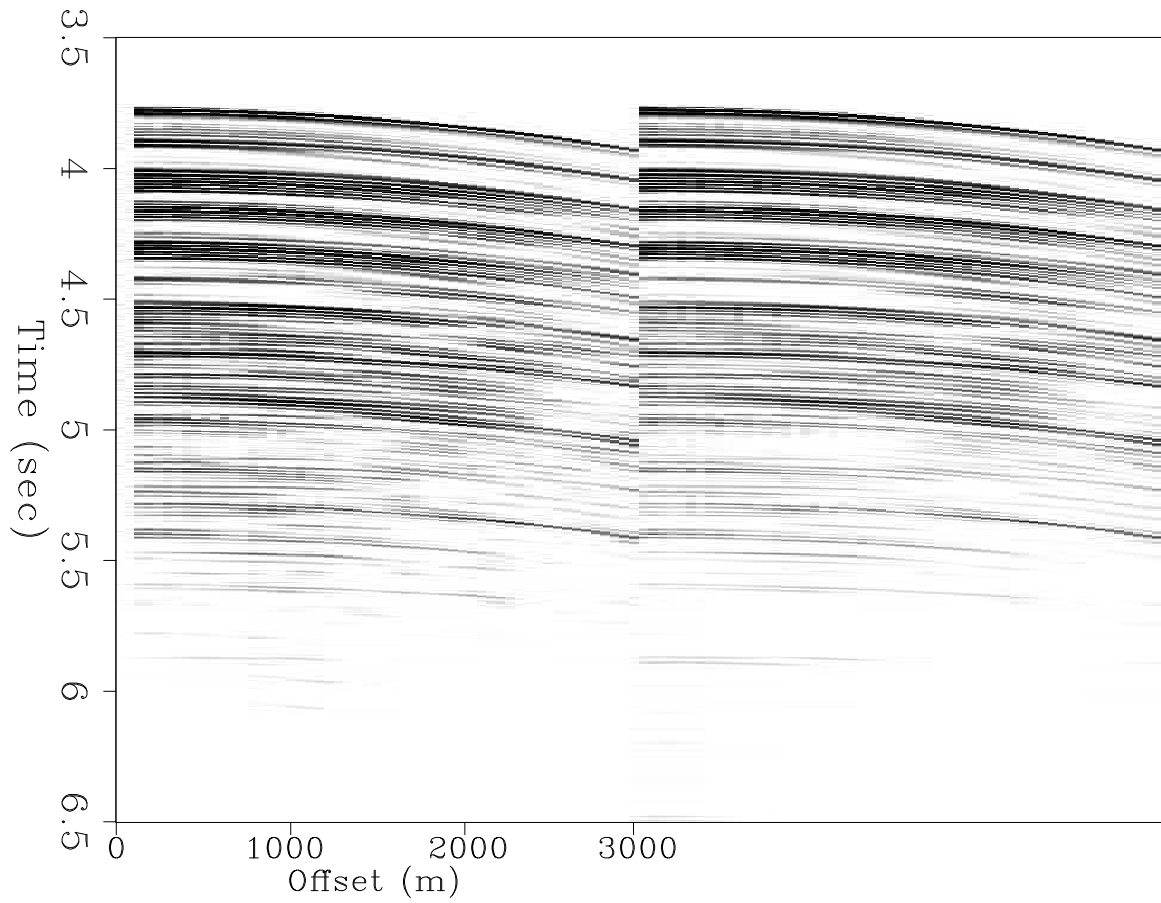


Figure 3.29: Crosstalk weights at CMP 55 of 750, before and after one nonlinear update. Left: Crosstalk weights before update. Right: Crosstalk weights after update. `results2d-crosstalk.gulf.iter` [CR,M]

coefficient, Figure 3.30 implicitly illustrates the beneficial change. The event highlighted in ovals on the residual panels, which has three visible peaks, does not have that wavelet shape in the raw data. Crosstalk between the overlapping events and an improperly high R1 reflection coefficient cause the event to be “manufactured” in the LSJIMP result. By better estimating the R1 reflection coefficient, the event is not present in the residual, and thus, not manufactured by LSJIMP. Other than this event, however, the differences between the two panels are minimal.

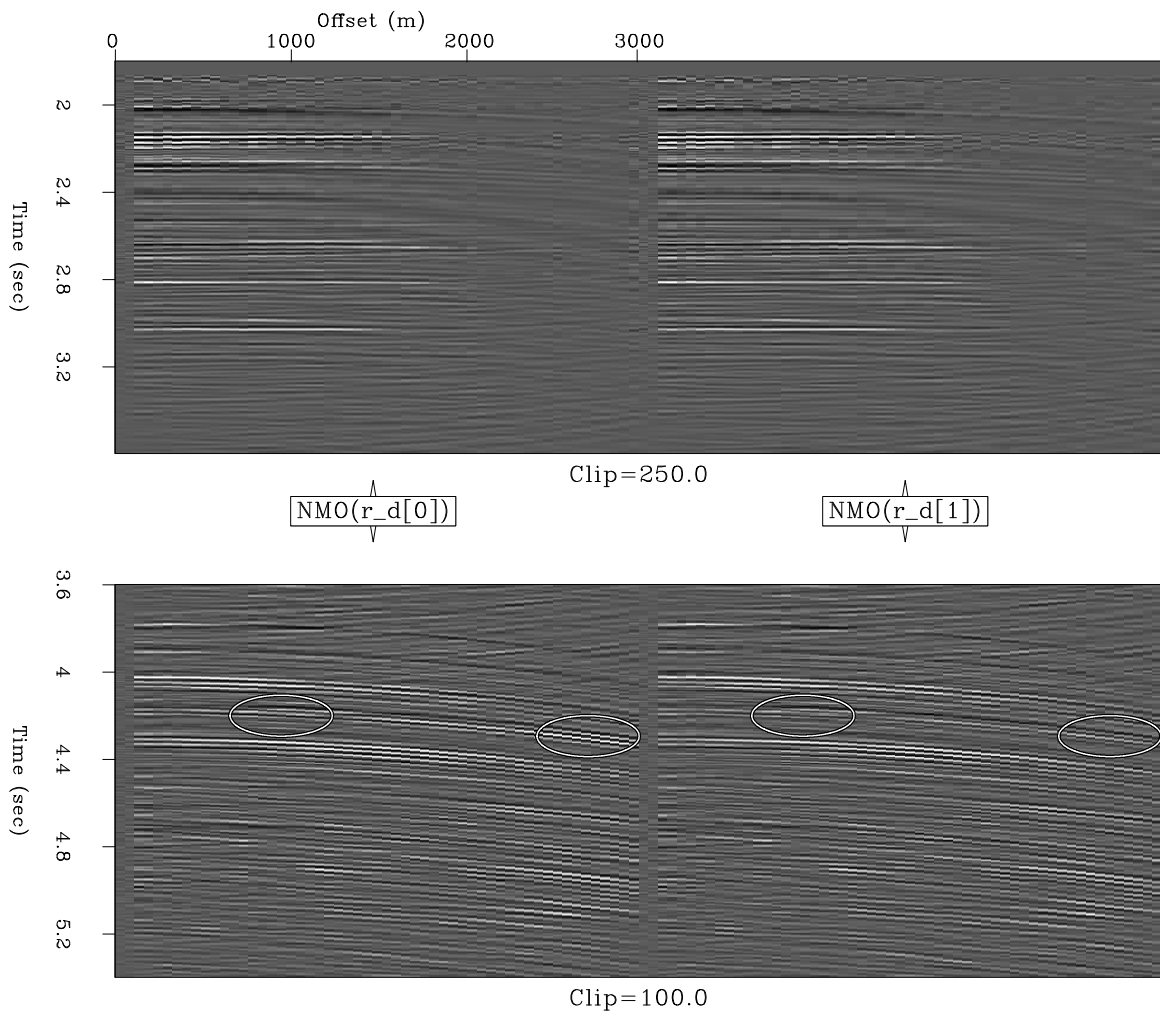


Figure 3.30: LSJIMP data residual before and after nonlinear update of crosstalk weights and reflection coefficients. Left: residual before updating. Right: residual after updating. Panels split in half along time axis for display purposes and clipped as labeled. `results2d-resd-iter1.gulf` [CR,M]

Figure 3.30 compares the LSJIMP estimated primaries at CMP 55 of 750 before and after the nonlinear update. The Figure is split in half along the time axis as explained earlier in section 3.0.2. Ovals highlight the same regions as were highlighted in Figure 3.30. The differences between the two estimated primary panels are quite subtle; the difference panel on the right is more enlightening. Notice how the manufactured event discussed earlier is better suppressed after the nonlinear update.

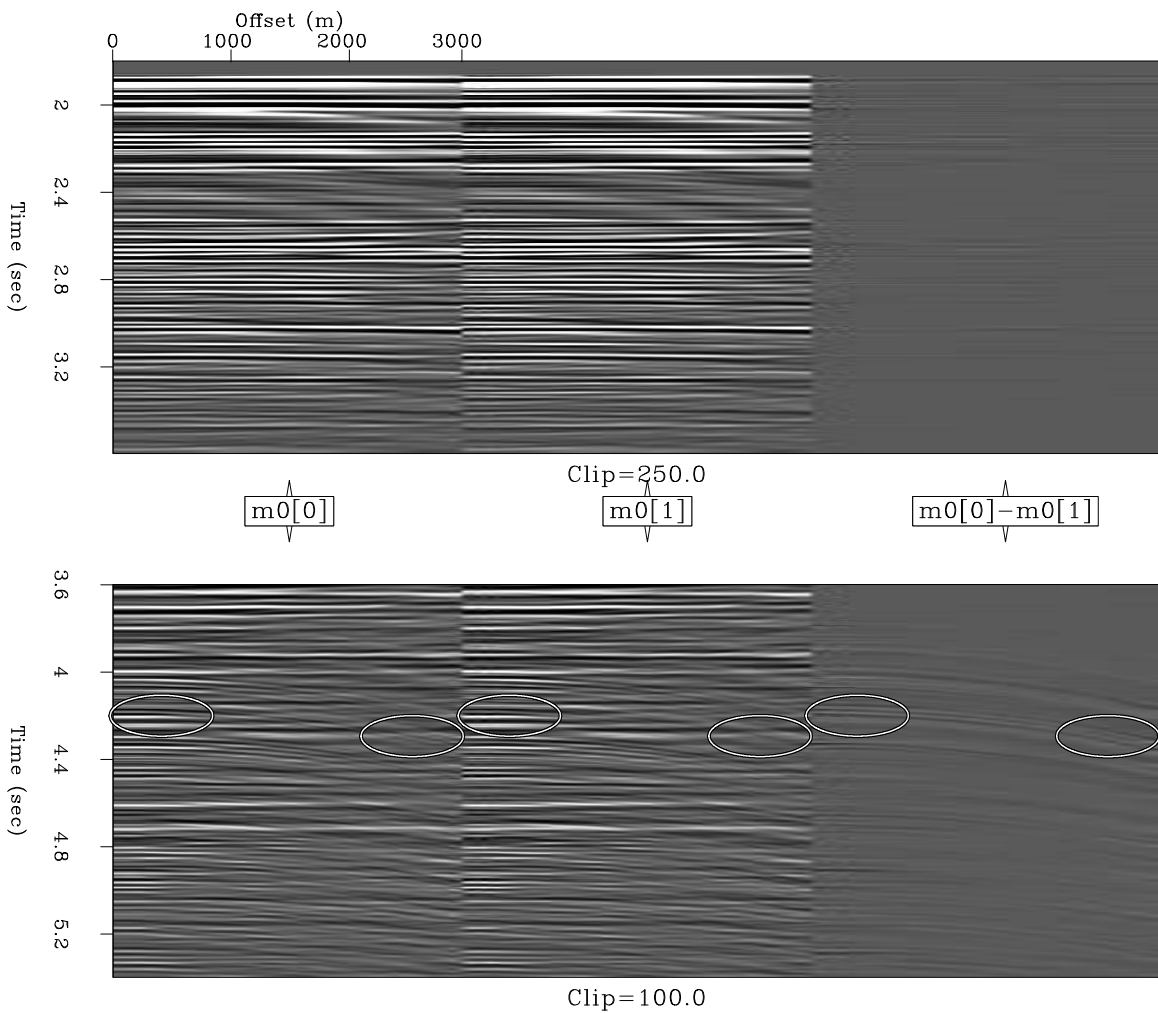


Figure 3.31: LSJIMP estimated primaries before and after nonlinear update of crosstalk weights and reflection coefficients. Left: m_0 before updating. Center: m_0 after updating. Right: Difference. Panels split in half along time axis for display purposes and clipped as labeled. `results2d-model-iter1.gulf` [CR,M]

Finally, Figure 3.32 shows the stack of the LSJIMP estimated primaries after the nonlinear update. The Figure is directly comparable with Figure 3.6. Again, the differences are quite subtle. Notice an improvement in the removal of deep, salt-related multiple events, like BSPLTS.

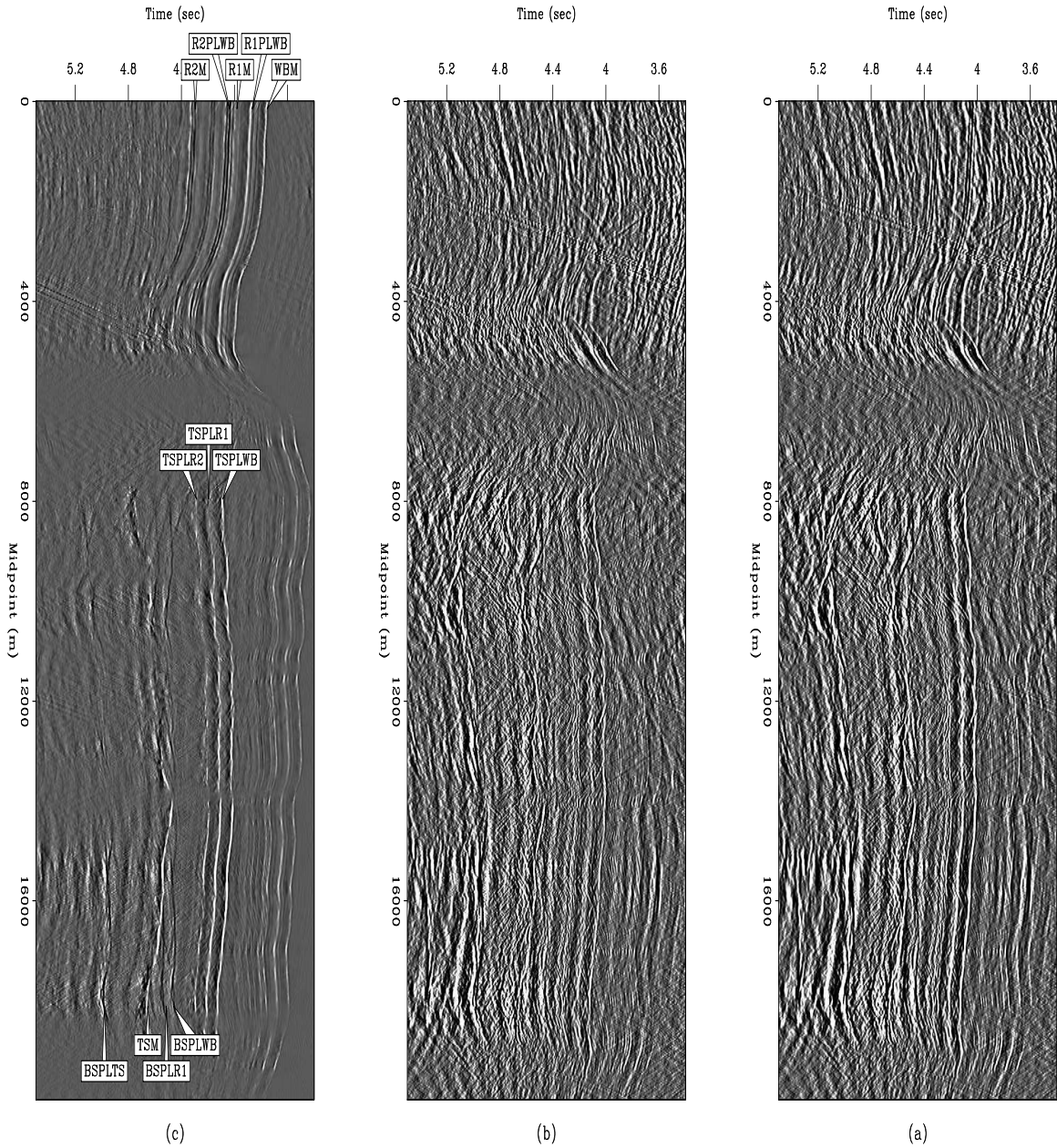


Figure 3.32: Top: raw data stack. Center: estimated LSJIMP primaries stack after nonlinear updating of crosstalk weights and reflection coefficients. Bottom: difference panel (estimated multiples) stack. Figure annotated and displayed with same gain and clip as Figure 3.6. `results2d-stackcomp-iter1.gulf` [CR,M]

Bibliography

- AAPG, 1998, Gulf of Mexico petroleum systems: AAPG Bulletin, **82**, no. 5.
- Berkhout, A. J., and Verschuur, D. J., 1994, Multiple technology: Part 2, migration of multiple reflections: Soc. of Expl. Geophys., 64th Ann. Internat. Mtg, 1497–1500.
- Berkhout, A. J., and Verschuur, D. J., 2003, Transformation of multiples into primary reflections: *in* 73rd Ann. Internat. Mtg Soc. of Expl. Geophys.
- Berryhill, J. R., and Kim, Y. C., 1986, Deep-water peglegs and multiples - Emulation and suppression: Geophysics, **51**, no. 12, 2177–2184.
- Biondi, B., and Palacharla, G., 1996, 3-D prestack migration of common-azimuth data: Geophysics, **61**, no. 06, 1822–1832.
- Biondi, B., Fomel, S., and Chemingui, N., 1998, Azimuth moveout for 3-D prestack imaging: Geophysics, **63**, no. 02, 574–588.
- Biondi, B., 1997, Azimuth moveout + common-azimuth migration: Cost-effective prestack depth imaging of marine data: Soc. of Expl. Geophys., 67th Ann. Internat. Mtg, 1375–1378.
- Brown, M., 2002, Simultaneous estimation of two slopes from seismic data, applied to signal/noise separation: SEP-**112**, 181–194.
- Claerbout, J. F., 1992, Earth Soundings Analysis: Processing Versus Inversion: Blackwell Scientific Publications.

- Claerbout, J. F., 1995, Basic Earth Imaging: Stanford Exploration Project.
- Fomel, S., 2001, Three-dimensional seismic data regularization: Ph.D. thesis, Stanford University.
- Fomel, S., 2002, Applications of plane-wave destruction filters: *Geophysics*, **67**, no. 06, 1946–1960.
- Foster, D. J., and Mosher, C. C., 1992, Suppression of multiple reflections using the Radon transform: *Geophysics*, **57**, no. 03, 386–395.
- Guitton, A., Brown, M., Rickett, J., and Clapp, R., 2001, Multiple attenuation using a t-x pattern-based subtraction method: *Soc. of Expl. Geophys.*, 71st Ann. Internat. Mtg, 1305–1308.
- Guitton, A., 2002, Shot-profile migration of multiple reflections: 72nd Ann. Internat. Mtg., *Soc. of Expl. Geophys.*, Expanded Abstracts, 1296–1299.
- Hampson, D., 1986, Inverse velocity stacking for multiple elimination: *J. Can. Soc. Expl. Geophys.*, **22**, no. 01, 44–55.
- Hargreaves, N., Wombell, R., and VerWest, B., 2003, Multiple attenuation using an apex-shifted radon transform: 65th Mtg., *Eur. Assoc. Geosc. Eng.*, Workshop: Strategies Towards Multi-Dimensional Multiple Attenuation.
- He, R., and Schuster, G., 2003, Least-squares migration of both primaries and multiples: *in* 73rd Ann. Internat. Mtg Soc. of Expl. Geophys.
- Hokstad, K., and Sollie, R., 2003, 3-D surface-related multiple elimination using parabolic sparse inversion: *in* 73rd Ann. Internat. Mtg Soc. of Expl. Geophys., 1961–1964.
- Hutchinson, M., and De Hoog, F., 1985, Smoothing noisy data with spline functions: Smoothing noisy data with spline functions: *Numer. Math.*, 99–106.
- Kabir, M. M. N., and Marfurt, K. J., 1999, Toward true amplitude multiple removal: *The Leading Edge*, **18**, no. 1, 66–73.

- Kleemeyer, G., Pettersson, S., Eppenga, R., Haneveld, C., Biersteker, J., and Den Ouden, R., 2003, It's magic – industry first 3D surface multiple elimination and pre-stack depth migration on Ormen Lange.; *in* 65th Mtg. Eur. Assn. Geosci. Eng., Session:B–43.
- Kuehl, H., and Sacchi, M., 2001, Generalized least-squares DSR migration using a common angle imaging condition: Soc. of Expl. Geophys., 71st Ann. Internat. Mtg, 1025–1028.
- Levin, F. K., and Shah, P. M., 1977, Peg-leg multiples and dipping reflectors: *Geophysics*, **42**, no. 05, 957–981.
- Levin, F. K., 1971, Apparent velocity from dipping interface reflections: *Geophysics*, **36**, no. 03, 510–516.
- Levin, S. A., 1996, AVO estimation using surface-related multiple prediction: Soc. of Expl. Geophys., 66th Ann. Internat. Mtg, 1366–1369.
- Lomask, J., 2003, Flattening 3D seismic cubes without picking: Soc. of Expl. Geophys., 73rd Ann. Internat. Mtg., 1402–1405.
- Lu, G., Ursin, B., and Lutro, J., 1999, Model-based removal of water-layer multiple reflections: *Geophysics*, **64**, no. 6, 1816–1827.
- Morley, L., 1982, Predictive multiple suppression: Ph.D. thesis, Stanford University.
- Nemeth, T., Wu, C., and Schuster, G. T., 1999, Least-squares migration of incomplete reflection data: *Geophysics*, **64**, no. 1, 208–221.
- Ottolini, R., 1982, Migration of reflection seismic data in angle-midpoint coordinates: Ph.D. thesis, Stanford University.
- Paffenholz, J., 2003, All-azimuth streamer acquisition: the impact on 3D multiple attenuation: 65th Mtg., Eur. Assoc. Geosc. Eng., Workshop: Strategies Towards Multi-Dimensional Multiple Attenuation.
- Prucha, M. L., and Biondi, B. L., 2002, Subsalt event regularization with steering filters: 72nd Ann. Internat. Mtg., Soc. of Expl. Geophys., Expanded Abstracts, 1176–1179.

- Prucha-Clapp, M., and Biondi, B., 2002, Subsalt event regularization with steering filters: Soc. of Expl. Geophys., 72nd Ann. Internat. Mtg, 1176–1179.
- Reiter, E. C., Toksoz, M. N., Keho, T. H., and Purdy, G. M., 1991, Imaging with deep-water multiples: *Geophysics*, **56**, no. 07, 1081–1086.
- Rickett, J., and Lumley, D. E., 2001, Cross-equalization data processing for time-lapse seismic reservoir monitoring: A case study from the Gulf of Mexico: *Geophysics*, **66**, no. 4, 1015–1025.
- Riley, D. C., and Claerbout, J. F., 1976, 2-D multiple reflections: *Geophysics*, **41**, no. 04, 592–620.
- Ross, W. S., Yu, Y., and Gasparotto, F. A., 1999, Traveltime prediction and suppression of 3-D multiples: *Geophysics*, **64**, no. 1, 261–277.
- Sacchi, M. D., and Ulrych, T. J., 1995, High-resolution velocity gathers and offset space reconstruction: *Geophysics*, **60**, no. 04, 1169–1177.
- Sava, P., and Fomel, S., 2000, Angle-gathers by Fourier Transform: *SEP*–**103**, 119–130.
- Sava, P., and Fomel, S., 2003, Angle-domain common-image gathers by wavefield continuation methods: *Geophysics*, **68**, no. 3, 1065–1074.
- Shan, G., 2003, Source-receiver migration of multiple reflections:, *in* 73rd Ann. Internat. Mtg Soc. of Expl. Geophys.
- Shuey, R. T., 1985, A simplification of the Zoeppritz-equations: *Geophysics*, **50**, no. 04, 609–614.
- Stoffa, P. L., Fokkema, J. T., de Luna Freire, R. M., and Kessinger, W. P., 1990, Split-step Fourier migration: *Geophysics*, **55**, no. 4, 410–421.
- Taner, M. T., and Koehler, F., 1969, Velocity spectra - Digital computer derivation and applications of velocity functions: *Geophysics*, **34**, no. 06, 859–881.

- Taner, M. T., 1980, Long-period sea-floor multiples and their suppression: *Geophys. Prosp.*, **28**, no. 01, 30–48.
- Tarantola, A., 1984, Inversion of seismic reflection data in the acoustic approximation: *Geophysics*, **49**, no. 08, 1259–1266.
- Thorson, J. R., and Claerbout, J. F., 1985, Velocity stack and slant stochastic inversion: *Geophysics*, **50**, no. 12, 2727–2741.
- Tsai, C. J., 1985, Use of autoconvolution to suppress first-order long-period multiples: Use of autoconvolution to suppress first-order long-period multiples: *Soc. of Expl. Geophys., Geophysics*, 1410–1425.
- Ursin, B., 1990, Offset-dependent geometrical spreading in a layered medium (short note): *Geophysics*, **55**, no. 04, 492–496.
- van Borstelen, R., 2003, Optimization of marine data acquisition for the application of 3D SRME: *in 73rd Ann. Internat. Mtg Soc. of Expl. Geophys.*, 1965–1968.
- van Dedem, E., and Verschuur, D., 2002, 3D surface-related multiple prediction using sparse inversion: experience with field data: *Soc. of Expl. Geophys., 72nd Ann. Internat. Mtg*, 2094–2097.
- Verschuur, D. J., Berkhout, A. J., and Wapenaar, C. P. A., 1992, Adaptive surface-related multiple elimination: *Geophysics*, **57**, no. 09, 1166–1177.
- Wang, J., Kuehl, H., and Sacchi, M. D., 2003, Least-squares wave-equation avp imaging of 3D common azimuth data: *in 73rd Ann. Internat. Mtg Soc. of Expl. Geophys.*
- Wang, Y., 2003, Multiple subtraction using an expanded multichannel matching filter: *Geophysics*, **68**, no. 1, 346–354.
- Wiggins, J. W., 1988, Attenuation of complex water-bottom multiples by wave equation-based prediction and subtraction: *Geophysics*, **53**, no. 12, 1527–1539.
- Yu, J., and Schuster, G., 2001, Crosscorrelogram migration of IVSPWD data: *Soc. of Expl. Geophys., 71st Ann. Internat. Mtg*, 456–459.